

# The role of viscosity on drop impact forces on non-wetting surfaces

Vatsal Sanjay<sup>1†</sup>, Bin Zhang<sup>2‡</sup>, Cunjing Lv<sup>2¶</sup>, and Detlef Lohse<sup>1,3||</sup>

<sup>1</sup>Physics of Fluids Group, Max Planck Center for Complex Fluid Dynamics, Department of Science and Technology, and J. M. Burgers Centre for Fluid Dynamics, University of Twente, P. O. Box 217, 7500 AE Enschede, The Netherlands

<sup>2</sup>Department of Engineering Mechanics, AML, Tsinghua University, Beijing 100084, China

<sup>3</sup>Max Planck Institute for Dynamics and Self-Organization, Am Fassberg 17, 37077 Göttingen, Germany

(Received xx; revised xx; accepted xx)

A liquid drop impacting a rigid substrate undergoes deformation and spreading due to normal reaction forces, which are counteracted by surface tension. On a non-wetting substrate, the drop subsequently retracts and takes off. Our recent work (Zhang et al., *Phys. Rev. Lett.*, vol. 129, 2022, 104501) revealed two peaks in the temporal evolution of the normal force  $F(t)$  – one at impact and another at jump-off. The second peak coincides with a Worthington jet formation, which vanishes at high viscosities due to increased viscous dissipation affecting flow focusing. In this article, using experiments, direct numerical simulations, and scaling arguments, we characterize both the peak amplitude  $F_1$  at impact and the one at take off ( $F_2$ ) and elucidate their dependency on the control parameters: the Weber number  $We$  (dimensionless impact kinetic energy) and the Ohnesorge number  $Oh$  (dimensionless viscosity). The first peak amplitude  $F_1$  and the time  $t_1$  to reach it depend on inertial timescales for low viscosity liquids, remaining nearly constant for viscosities up to 100 times that of water. For high viscosity liquids, we balance the rate of change in kinetic energy with viscous dissipation to obtain new scaling laws:  $F_1/F_\rho \sim \sqrt{Oh}$  and  $t_1/\tau_\rho \sim 1/\sqrt{Oh}$ , where  $F_\rho$  and  $\tau_\rho$  are the inertial force and time scales, respectively, which are consistent with our data. The time  $t_2$  at which the amplitude  $F_2$  appears is set by the inertio-capillary timescale  $\tau_\gamma$ , independent of both the viscosity and the impact velocity of the drop. However, these properties dictate the magnitude of this amplitude.

**Key words:**

---

## 1. Introduction

Drop impacts have piqued the interest of scientists and artists alike for centuries, with the phenomenon being sketched by da Vinci (1508) in the early 16<sup>th</sup> and photographed by Worthington (1876a,b) in the late 19<sup>th</sup> century. It is, indeed, captivating to observe raindrops hitting a solid surface (Kim et al. 2020; Lohse & Villermaux 2020) or ocean

† Email address for correspondence: vatsalsanjay@gmail.com

‡ Email address for correspondence: binzhang0710@gmail.com

¶ Email address for correspondence: cunjinglv@mail.tsinghua.edu.cn

|| Email address for correspondence: d.lohse@utwente.nl

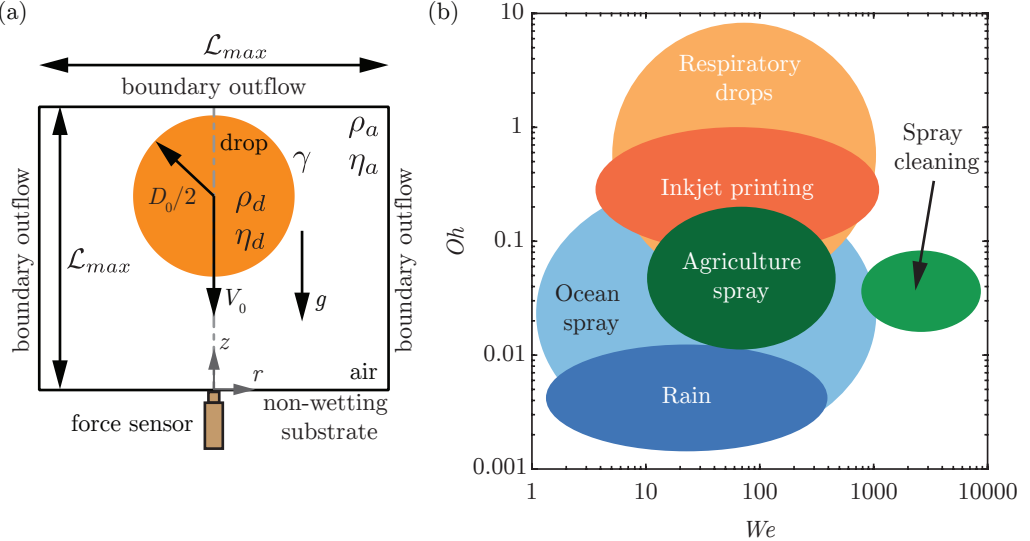


FIGURE 1. (a) Problem schematic with an axisymmetric computational domain used to study the impact of a drop with diameter  $D_0$  and velocity  $V_0$  on a non-wetting substrate. In the experiments, we use a quartz force sensor to measure the temporal variation of the impact force. The subscripts  $d$  and  $a$  denote the drop and air, respectively, to distinguish their material properties, which are the density  $\rho$  and the dynamic viscosity  $\eta$ . The drop-air surface tension coefficient is  $\gamma$ . The grey dashed-dotted line represents the axis of symmetry,  $r = 0$ . Boundary air outflow is applied at the top and side boundaries (tangential stresses, normal velocity gradient, and ambient pressure are set to zero). The domain boundaries are far enough from the drop not to influence its impact process ( $L_{\max} \gg D_0$ ,  $L_{\max} = 8R$  in the worst case). (b) The phase space with control parameters: the Weber number ( $We$ : dimensionless kinetic energy) and the Ohnesorge number ( $Oh$ : dimensionless viscosity), exemplifying different applications.

spray affecting maritime structures (Berny *et al.* 2021; Villermaux *et al.* 2022). The phenomenology of drop impact is extremely rich, encompassing behaviors such as drop deformation (Biance *et al.* 2006; Moláček & Bush 2012; Chevy *et al.* 2012), spreading (Laan *et al.* 2014; Wildeman *et al.* 2016), splashing (Xu *et al.* 2005; Riboux & Gordillo 2014; Thoraval *et al.* 2021), fragmentation (Villermaux & Bossa 2011; Villermaux 2020), bouncing (Richard & Quéré 2000; Kolinski *et al.* 2014; Jha *et al.* 2020; Chubynsky *et al.* 2020; Sharma & Dixit 2021; Sanjay *et al.* 2023a), and wetting (de Gennes 1985; Fukai *et al.* 1995; Quéré 2008; Bonn *et al.* 2009). These behaviors are influenced by the interplay of inertial, capillary, and viscous forces, as well as additional factors like non-Newtonian properties (Bartolo *et al.* 2005, 2007; Smith & Bertola 2010; Gorin *et al.* 2022) of the liquid and even ambient air pressure (Xu *et al.* 2005), making the parameter space for this phenomenon both extensive and high-dimensional.

Naturally, even the process of a Newtonian liquid drop impacting a rigid substrate is governed by a plethora of control parameters, including but not limited to the drop's density  $\rho_d$ , diameter  $D_0$ , velocity  $V_0$ , dynamic viscosity  $\eta_d$ , surface tension  $\gamma$ , and acceleration due to gravity  $g$  (figure 1a). To navigate this rich landscape, we focus on two main dimensionless numbers that serve as control parameters (figure 1b): the Weber number  $We$ , which is the ratio of inertial to capillary forces and is given by

$$We = \frac{\rho_d V_0^2 D_0}{\gamma}, \quad (1.1)$$

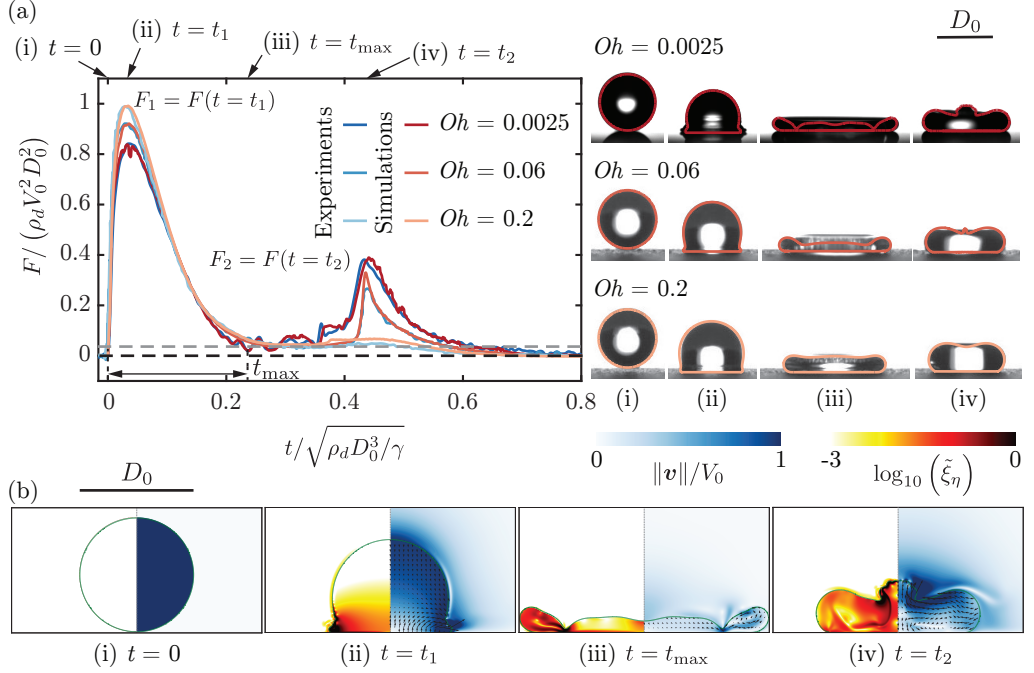


FIGURE 2. Comparison of the drop impact force  $F(t)$  obtained from experiments and simulations for the three typical cases with impact velocity  $V_0 = 1.2 \text{ m/s}, 0.97 \text{ m/s}, 0.96 \text{ m/s}$ , diameter  $D_0 = 2.05 \text{ mm}, 2.52 \text{ mm}, 2.54 \text{ mm}$ , surface tension  $\gamma = 72 \text{ mN/m}, 61 \text{ mN/m}, 61 \text{ mN/m}$  and viscosity  $\eta_d = 1 \text{ mPa s}, 25.3 \text{ mPa s}, 80.2 \text{ mPa s}$ . These parameter give  $Oh = 0.0025, 0.06, 0.2$  and  $We = 40$ . For the three cases, the two peak amplitudes,  $F_1 / (\rho_d V_0^2 D_0^2) \approx 0.82, 0.92, 0.99$  at  $t_1 \approx 0.03\sqrt{\rho_d D_0^3 / \gamma}$  and  $F_2 / (\rho_d V_0^2 D_0^2) \approx 0.37, 0.337, 0.1$  at  $t_2 \approx 0.42\sqrt{\rho_d D_0^3 / \gamma}$ , characterize the inertial shock from impact and the Worthington jet before takeoff, respectively. The drop reaches the maximum spreading at  $t_{\max}$  when it momentarily stops and retracts until  $0.8\sqrt{\rho_d D_0^3 / \gamma}$  when the drop takes off ( $F = 0$ ). The black and gray dashed lines in panel (a) mark  $F = 0$  and the resolution  $F = 0.5 \text{ mN}$  of our piezoelectric force transducer, respectively. (b) Four instances are further elaborated through numerical simulations for ( $We = 40, Oh = 0.0025$ ), namely (i)  $t = 0$  (touch-down), (ii)  $t = 0.03\sqrt{\rho_d D_0^3 / \gamma}$  ( $t_1$ ), (iii)  $t = 0.2\sqrt{\rho_d D_0^3 / \gamma}$  ( $t_{\max}$ ), and (iv)  $t = 0.42\sqrt{\rho_d D_0^3 / \gamma}$  ( $t_2$ ). The insets of panel (a) exemplify these four instances for the three representative cases illustrated here. The experimental snapshots are overlaid with the drop boundaries from simulations. We stress the excellent agreement between experiments and simulations without any free parameters. The left part of each numerical snapshot shows (on a  $\log_{10}$  scale) the dimensionless local viscous dissipation function  $\xi_\eta \equiv \xi_\eta D_0 / (\rho_d V_0^3) = 2Oh (\mathcal{D} : \tilde{\mathcal{D}})$ , where  $\mathcal{D}$  is the symmetric part of the velocity gradient tensor, and the right part the velocity field magnitude normalized with the impact velocity. The black velocity vectors are plotted in the center of mass reference frame of the drop to clearly elucidate the internal flow. Also see supplementary videos SM1-SM3.

and the Ohnesorge number  $Oh$ , which captures the interplay between viscous damping and capillary oscillations, offering insights into how viscosity affects the drop's behavior upon impact,

$$Oh = \frac{\eta_d}{\sqrt{\rho_d \gamma D_0}}. \quad (1.2)$$

Additionally, the Bond number

$$Bo = \frac{\rho_d g D_0^2}{\gamma} \quad (1.3)$$

58 compares gravity to inertial forces and is needed to uniquely define the non-dimensional  
 59 problem.

60 The drop impact is not only interesting from the point of view of fundamental research  
 61 but also finds relevance in inkjet printing (Lohse 2022), the spread of respiratory drops  
 62 carrying airborne microbes (Bourouiba 2021; Ji *et al.* 2021; Pöhlker *et al.* 2023), cooling  
 63 applications (Kim 2007; Shiri & Bird 2017; Jowkar & Morad 2019), agriculture (Bergeron  
 64 *et al.* 2000; Bartolo *et al.* 2007; Kooij *et al.* 2018; Sijs & Bonn 2020; He *et al.* 2021;  
 65 Hoffman *et al.* 2021), criminal forensics (Smith *et al.* 2018; Smith & Brutin 2018), and  
 66 many other industrial and natural processes (Rein 1993; Yarin 2006; Tuteja *et al.* 2007;  
 67 Cho *et al.* 2016; Josserand & Thoroddsen 2016; Yarin *et al.* 2017; Liu *et al.* 2017; Hao  
 68 *et al.* 2016; Yarin *et al.* 2017; Wu *et al.* 2020). For these applications, it is pertinent to  
 69 understand the forces involved in drop impacts, as these forces can lead to soil erosion  
 70 (Nearing *et al.* 1986) or damage to engineered surfaces (Ahmad *et al.* 2013; Amirzadeh  
 71 *et al.* 2017; Gohardani 2011). We refer the readers to Cheng *et al.* (2022) for an overview  
 72 of the recent studies unraveling drop impact forces; see also Li *et al.* (2014); Soto *et al.*  
 73 (2014); Philippi *et al.* (2016); Zhang *et al.* (2017); Gordillo *et al.* (2018); Mitchell *et al.*  
 74 (2019); Zhang *et al.* (2019).

75 These forces have been studied by Zhang *et al.* (2022), employing experiments and  
 76 simulations and deriving scaling laws. A liquid drop impacting a non-wetting substrate  
 77 undergoes a series of phases—spreading, recoiling, and potentially rebounding (Chantelot  
 78 2018)—driven by the normal reaction force exerted by the substrate (figure 2). The  
 79 moment of touch-down (see figures 2a,b  $t = 0$  to  $t_1$ ) (Wagner 1932; Philippi *et al.* 2016;  
 80 Gordillo *et al.* 2018) is not surprisingly associated with a pronounced peak in the temporal  
 81 evolution of the drop impact force  $F(t)$  owing to the sudden deceleration as high as 100  
 82 times the acceleration due to gravity (Clanet *et al.* 2004) (figure 2a,  $F_1/(\rho_d V_0^2 D_0^2) \approx 0.82$ ,  
 83 0.92, 0.99 for  $Oh = 0.0025, 0.06$ , and  $0.2$ , respectively; at  $t_1 \approx 0.03\sqrt{\rho_d D_0^3/\gamma}$ . The force  
 84 diminishes as the drop reaches its maximum spreading diameter (figure 2a,b  $t = t_m$ ).  
 85 Zhang *et al.* (2022) revealed that also the jump-off is accompanied by a peak in the normal  
 86 reaction force, which was up to then unknown (figure 2a,  $F_2/(\rho_d V_0^2 D_0^2) \approx 0.37, 0.337$ ,  
 87 0.1 for  $Oh = 0.0025, 0.06$ , and  $0.2$ , respectively; for the second force peak amplitude—at  
 88 time  $t_2 \approx 0.42\sqrt{\rho_d D_0^3/\gamma}$  after impact) The second peak in the force also coincides with  
 89 the formation of a Worthington jet, a narrow upward jet of liquid that can form due  
 90 to flow focusing by the retracting drop (figure 2a,b  $t = t_2$ ). Under certain conditions  
 91 ( $We \approx 9$ ,  $Oh = 0.0025$ ), this peak can be even more pronounced than the first. This  
 92 discovery is critical for superhydrophobicity which is volatile and can fail due to external  
 93 disturbances such as pressure (Lafuma & Quéré 2003; Callies & Quéré 2005; Sbragaglia  
 94 *et al.* 2007; Li *et al.* 2017), evaporation (Tsai *et al.* 2010; Chen *et al.* 2012; Papadopoulos  
 95 *et al.* 2013), mechanical vibration (Bormashenko *et al.* 2007), or the impact forces of  
 96 prior droplets (Bartolo *et al.* 2006a).

97 In contrast to our prior study Zhang *et al.* (2022), which fixed the Ohnesorge number  
 98 to that of a 2 mm diameter water drop ( $Oh = 0.0025$ ), our present investigation reported  
 99 in this paper explores a broader parameter space. We systematically and independently  
 100 vary the Weber and Ohnesorge numbers, extending the range of  $Oh$  to as high as 100.  
 101 This comprehensive approach enables us to develop new scaling laws and provides a  
 102 more unified understanding of the forces involved in drop impact problems. Our findings

glycerol (wt %)	$\rho_d$ (kg/m <sup>3</sup> )	$\eta_d$ (mPa.s)	$\gamma$ (mN/m)
0	1000	1	72
50	1124	5	61
63	1158	10	61
74	1188	25.3	61
80	1200	45.4	61
85	1220	80.2	61

TABLE 1. Properties of the water-glycerol mixtures used in the experiments.  $\rho_d$  and  $\eta_d$  are the density and viscosity of the drop, respectively and  $\gamma$  denotes the liquid-air surface tension coefficient. These properties are calculated using the protocol provided in [Cheng \(2008\)](#); [Volk & Kähler \(2018\)](#).

103 are particularly relevant for applications with varying viscosities and impact velocities  
104 (figure 1).

105 The structure of this paper is as follows: §2 briefly describes the experimental and  
106 numerical methods. §3 and §4 offer detailed analyses of the first and second peaks,  
107 respectively, focusing on their relationships with the Weber number ( $We$ ) and the  
108 Ohnesorge number ( $Oh$ ). Conclusions and perspectives for future research are presented  
109 in Section 5.

## 110 2. Methods

### 111 2.1. Experimental method

112 In the experimental setup, shown schematically in figure 1(a), a liquid drop impacts a  
113 superhydrophobic substrate. For water drops, such a surface is coated with silanized silica  
114 nanobeads with a diameter of 20 nm (Glaco Mirror Coat Zero; Soft99) resulting in the  
115 advancing and receding contact angles of  $167 \pm 2^\circ$  and  $154 \pm 2^\circ$ , respectively ([Gauthier  
116 et al. 2015](#); [Li et al. 2017](#)). On the other hand, for viscous aqueous glycerin drops,  
117 the upper surface is coated with an acetone solution of hydrophobic beads (Ultra ever  
118 Dry, Ultratech International, a typical bead size of 20 nm), resulting in the advancing  
119 and receding contact angles of  $166 \pm 4^\circ$  and  $159 \pm 2^\circ$ , respectively ([Jha et al. 2020](#)).  
120 The properties of the impacting drop are controlled using water-glycerol mixtures with  
121 viscosities  $\eta_d$  varying by almost two orders of magnitude, from 1 mPas to 80.2 mPas.  
122 Surface tension is either 72 mN/m (pure water) or 61 mN/m (glycerol), while density  
123  $\rho_d$  ranges from 1000 kg/m<sup>3</sup> to 1220 kg/m<sup>3</sup>, as detailed in table 1 ([Cheng 2008](#); [Volk  
124 & Kähler 2018](#); [Jha et al. 2020](#)). We note that using liquids such as silicone oil can  
125 provide a broader range of viscosity variation when paired with a superamphiphobic  
126 substrate ([Deng et al. 2012](#)). Additionally, employing drops of smaller radii facilitates  
127 the exploration of higher Ohnesorge numbers ( $Oh$ , see (1.2)). The drop diameter  $D_0$  is  
128 controlled between 2.05 mm and 2.76 mm by pushing it through a calibrated needle (see  
129 appendix A for details). Consequently, we calculate  $Oh$  using the properties in table 1.  
130 The Weber number ( $We$ , see (1.1)) is set using the impact velocity  $V_0$  varying between  
131 0.38 m/s and 2.96 m/s by changing the release height of the drops above the substrate.  
132 All experiments are conducted at ambient pressure and temperature. The impact force  
133 is directly measured using a high-precision piezoelectric force transducer (Kistler 9215A)  
134 with a resolution of 0.5 mN. During these measurements, the high-frequency vibrations  
135 induced by the measurement system and the surrounding noise are spectrally removed

136 using a low pass filter with a cut-off frequency of 5 kHz, following the procedure in Li *et al.*  
 137 (2014); Zhang *et al.* (2017); Gordillo *et al.* (2018); Mitchell *et al.* (2019). The experiment  
 138 also employs a high-speed camera (Photron Fastcam Nova S12) synchronized at 10,000  
 139 fps with a shutter speed 1/20,000 s. Throughout the manuscript, the error bars are of  
 140 statistical nature (one standard deviation) and originate from repeated trials. They are  
 141 visible if they are larger than the marker size. We refer the readers to the supplementary  
 142 material of Zhang *et al.* (2022) and appendix A for further details of the experimental  
 143 setup and error characterization of the dimensionless control parameters.

## 144 2.2. Numerical framework

145 In the direct numerical simulations (DNS) employed for this study, the continuity and  
 146 the momentum equations take the form

$$\nabla \cdot \mathbf{v} = 0 \quad (2.1)$$

147 and

$$\frac{\partial \mathbf{v}}{\partial t} + \nabla \cdot (\mathbf{v} \mathbf{v}) = \frac{1}{\rho} (-\nabla p + \nabla \cdot (2\eta \mathcal{D}) + \mathbf{f}_\gamma) + \mathbf{g}, \quad (2.2)$$

148 respectively. Here,  $\mathbf{v}$  is the velocity field,  $t$  is time,  $p$  is pressure, and  $\mathbf{g}$  is acceleration  
 149 due to gravity. We use the free software program *Basilisk C* that employs the well-  
 150 balanced geometric volume of fluid (VoF) method (Popinet 2009, 2018). The VoF tracer  
 151  $\Psi$  delineates the interface between the drop (subscript  $d$ ,  $\psi = 1$ ) and air (subscript  $a$ ,  
 152  $\psi = 0$ ), introducing a singular force  $\mathbf{f}_\gamma \approx \gamma \kappa \nabla \Psi$  ( $\kappa$  denotes interfacial curvature, see  
 153 Brackbill *et al.* 1992) to respect the dynamic boundary condition at the interface. This  
 154 VoF tracer sets the material properties such that density  $\rho$  and viscosity  $\eta$  are given by

$$\rho = \rho_a + (\rho_d - \rho_a) \Psi \quad (2.3)$$

155 and

$$\eta = \eta_a + (\eta_d - \eta_a) \Psi, \quad (2.4)$$

156 respectively. This VoF field is advected with the flow, following the equation

$$\frac{\partial \Psi}{\partial t} + \nabla \cdot (\mathbf{v} \Psi) = 0. \quad (2.5)$$

157 Lastly, we calculate the normal reaction force  $\mathbf{F}(t)$  by integrating the pressure field  $p$  at  
 158 the substrate,

$$\mathbf{F}(t) = \left( \int_{\mathcal{A}} (p - p_0) d\mathcal{A} \right) \hat{\mathbf{z}}, \quad (2.6)$$

159 where,  $p_0$ ,  $d\mathcal{A}$ , and  $\hat{\mathbf{z}}$  are the ambient pressure, substrate area element, and the unit  
 160 vector normal to the substrate, respectively.

161 We leverage the axial symmetry of the drop impact (figure 1a). This axial symmetry  
 162 breaks at large  $We$  ( $\geq 100$  for water drops and even larger Weber number for more  
 163 viscous drops), owing to destabilization by the surrounding gas after splashing (Xu *et al.*

2005; Eggers *et al.* 2010; Driscoll & Nagel 2011; Riboux & Gordillo 2014; Josserand & Thoroddsen 2016; Zhang *et al.* 2022). To solve the governing equations (2.1)-(2.5), the velocity field  $\mathbf{v}$  and time  $t$  are normalized by the inertio-capillary scales,  $V_\gamma = \sqrt{\gamma/\rho_d D_0}$  and  $\tau_\gamma = \sqrt{\rho_d D_0^3/\gamma}$ , respectively. Furthermore, the pressure is normalized using the capillary pressure scale  $p_\gamma = \gamma/D_0$ . In such a conceptualization,  $Oh$  and  $We$  described in §1 uniquely determine the system. The Ohnesorge number based on air viscosity  $Oh_a = (\eta_a/\eta_d) Oh$  and air-drop density ratio  $\rho_a/\rho_d$  are fixed at  $10^{-5}$  and  $10^{-3}$ , respectively to minimize the influence of the surrounding medium on the impact forces. Lastly, we keep the Bond number  $Bo$  (see (1.3)) fixed at 1 throughout the manuscript. In our system, the relevance of gravity is characterized by the dimensionless Froude number  $Fr = V_0^2/(gD_0) = We/Bo$  which compares inertia with gravity. Throughout this manuscript,  $Fr > 1$  and gravity's role is sub-dominant compared to inertia (for detailed discussion, see appendix B). The substrate is modeled as a no-slip and non-penetrable wall, whereas vanishing stress and pressure are applied at the remaining boundaries to mimic outflow conditions for the surrounding air. The domain boundaries are far enough from the drop not to influence its impact process ( $\mathcal{L}_{\max} \gg D_0$ ,  $\mathcal{L}_{\max} = 8R$  in the worst case). At  $t = 0$ , in our simulations, we release a spherical drop whose south pole is  $0.05D_0$  away from the substrate and is falling with a velocity  $V_0$ . It is important to note that large experimental drops may deviate from perfect sphericity due to air drag as they fall after detaching from the needle and potential residual oscillations from detachment. These shape perturbations are more pronounced in cases with low Weber and Ohnesorge numbers. To quantify this non-sphericity, we measure the drop's aspect ratio (horizontal to vertical diameter) immediately before substrate contact. The precise pre-impact drop shape can significantly influence subsequent impact dynamics (Thoraval *et al.* 2013; Yun 2017; Zhang *et al.* 2019). In our experiments, we constrain our analysis to drops with aspect ratios between 0.96 and 1.05. Given this narrow range, we posit that the impact of these shape variations is negligible compared to the experimental error bars derived from repeated trials under identical nominal conditions. The simulations utilize adaptive mesh refinement to finely resolve the velocity, viscous dissipation, and the VoF tracer fields. A minimum grid size  $\Delta = D_0/2048$  is used for this study.

To ensure a perfectly non-wetting surface, we impose a thin air layer (minimum thickness  $\sim \Delta/2$ ) between the drop and the substrate. This air layer prevents direct contact between the liquid and solid (Kolinski *et al.* 2014; Sprittles 2024), effectively mimicking a perfectly non-wetting surface. The presence of this air layer is crucial for capturing the dynamics of drop impact on superhydrophobic surfaces, as it allows for the formation of an air cushion that can significantly affect the spreading and rebound behavior of the drop (Ramírez-Soto *et al.* 2020; Sanjay *et al.* 2023a). While this approach does not fully resolve the microscopic dynamics within the air layer itself, such as the high-velocity gradients and viscous dissipation inside the gas film once it thins below a critical size ( $\sim 10\Delta$ ), it has been shown to accurately capture the macroscopic behavior of drop impact in the parameter range of interest (Ramírez-Soto *et al.* 2020; Sanjay *et al.* 2023b; Alventosa *et al.* 2023a; García-Geijo *et al.* 2024). We refer the readers to Sanjay (2022) for discussions about this “precursor”, air film method and to Popinet & collaborators (2013–2023); Sanjay (2024); Zhang *et al.* (2022) for details on the numerical framework.

### 209 3. Anatomy of the first impact force peak

210 This section elucidates the anatomy of the first impact force peak and its relationship  
 211 with the Weber  $We$  and Ohnesorge  $Oh$  numbers, first for the inertial limit (§3.1,  $Oh \ll 1$ )

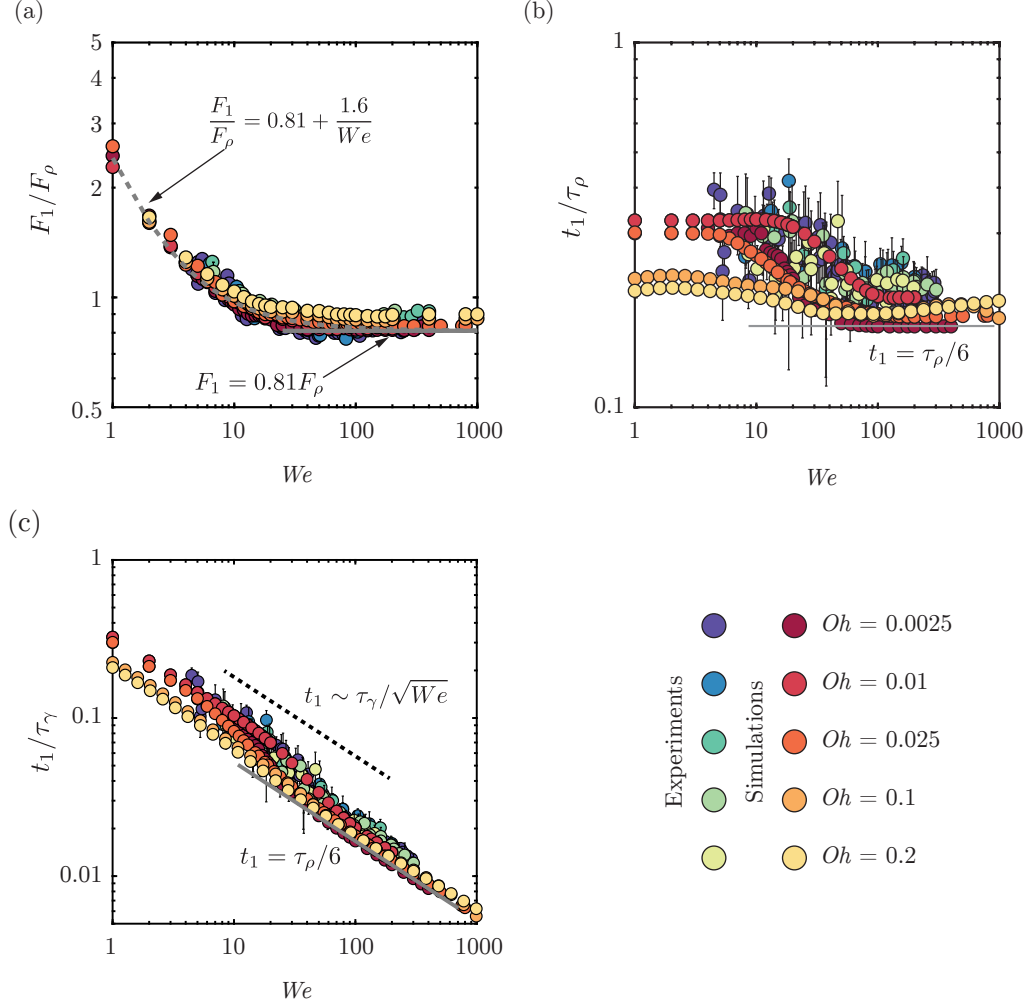


FIGURE 3. Anatomy of the first impact force peak amplitude at low  $Oh$  in between 0.0025 and 0.2, see color legend:  $We$  dependence of the (a) magnitude  $F_1$  normalized by the inertial force scale  $F_\rho = \rho_d V_0^2 D_0^2$  and time  $t_1$  to reach the first force peak amplitude normalized by (b) the inertial timescale  $\tau_\rho = D_0/V_0$  and (c) the inertia-capillary time scale  $\tau_\gamma = \sqrt{\rho_d D_0^3/\gamma}$ .

212 and then for the viscous asymptote (§3.2,  $Oh \gg 1$ ). The results of this section are  
 213 summarized in figure 3 that shows an excellent agreement between experiments and  
 214 simulations without any free parameters.

### 215 3.1. Low Ohnesorge number impacts

216 For low  $Oh$  and large  $We$ , inertial force and time scales dictate the drop impact  
 217 dynamics (figures 3 and 4). As the drop falls on a substrate, the part of the drop  
 218 immediately in contact with the substrate stops moving, whereas the top of the drop  
 219 still falls with the impact velocity (figure 4, from  $t = t_1/4$  until  $t = t_1$ ). Consequently,  
 220 momentum conservation implies

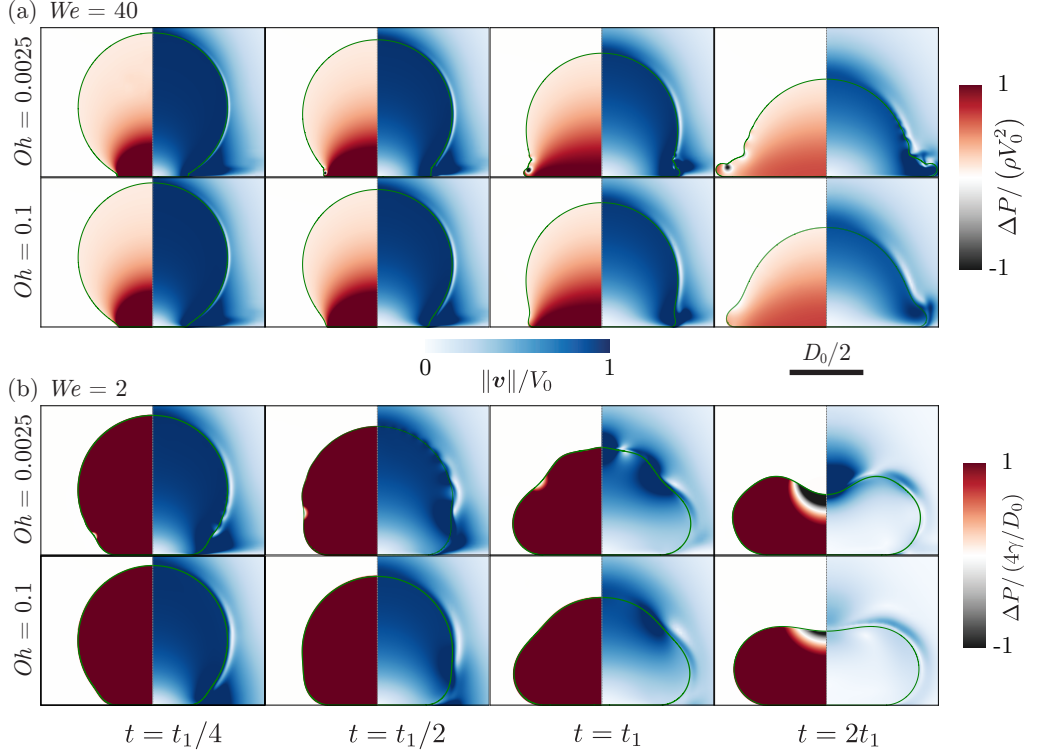


FIGURE 4. Direct numerical simulations snapshots illustrating the drop impact dynamics for  $We =$  (a) 40 and (b) 2. The left-hand side of each numerical snapshot shows the pressure normalized by (a) the inertial pressure scale  $\rho_d V_0^2$  and (b) the capillary pressure scale  $\gamma/D_0$ . The right-hand side shows the velocity field magnitude normalized by the impact velocity  $V_0$ .

$$F_1 \sim V_0 \frac{dm}{dt}, \quad (3.1)$$

where the mass flux  $dm/dt \sim \rho_d V_0 D_0^2$  (Soto *et al.* 2014; Zhang *et al.* 2022). As a result, the first peak amplitude scales with the inertial pressure force (figure 3a)

$$F_1 \sim F_\rho, \text{ where } F_\rho = \rho_d V_0^2 D_0^2, \quad (3.2)$$

for high Weber numbers ( $We > 30$ ,  $F_1 \approx 0.81 F_\rho$ ). Furthermore, the time  $t_1$  to reach  $F_1$  follows

$$t_1 \sim \frac{D_0}{V_0} = \tau_\rho, \quad (3.3)$$

where,  $\tau_\rho$  is the inertial timescale. The relation between equations (3.2) and (3.3) is apparent from the momentum conservation which implies that the impulse of the first force peak is equal to the momentum of the impacting drop, i.e.,  $F_1 t_1 \sim \rho_d V_0 D_0^3 = F_\rho \tau_\rho$  (see Gordillo *et al.* 2018, Zhang *et al.* 2022, and figures 3b,c). These scaling laws depend only on the inertial shock at impact and are wettability-independent (Zhang *et al.* 2017; Gordillo *et al.* 2018; Zhang *et al.* 2022). For details of the scaling law, including the

prefactors, we refer the readers to [Philippi et al. \(2016\)](#); [Gordillo et al. \(2018\)](#); [Cheng et al. \(2022\)](#).

Figure 3 further illustrates that this inertial asymptote is insensitive to viscosity variations up to 100-fold as  $F_1 \sim F_\rho$  and  $t_1 \sim \tau_\rho$  for  $0.0025 < Oh < 0.2$ . However, deviations from the inertial force and time scales are apparent for  $We < 30$  (figure 3), a phenomenon also reported in earlier work ([Soto et al. 2014](#); [Zhang et al. 2022](#)). In these instances, inertia does not act as the sole governing force but instead complements surface tension, which dictates the pressure inside the drop ( $p \sim \gamma/D_0$  throughout the drop for  $We \lesssim 1$ , figure 4b). [Zhang et al. \(2022\)](#) proposed an empirical functional dependence as

$$F_1 = \left( \alpha_1 \rho_d V_0^2 + \alpha_2 \frac{\gamma}{D_0} \right) D_0^2, \quad (3.4)$$

based on dimensional analysis, with  $\alpha_1$  and  $\alpha_2$  as free parameters which were determined to be approximately 1.6 and 0.81, respectively for water ( $Oh = 0.0025$ ). These coefficients only deviate marginally in the current work despite the significant increase in  $Oh$  as compared to previous works ([Cheng et al. 2022](#); [Zhang et al. 2022](#)). This consistency underscores the invariance of the pressure field inside the drop to an increase in  $Oh$  (close to the impact region, figure 4a and throughout the drop, figure 4b).

### 3.2. Large Ohnesorge number impacts

Figure 5 reaffirms the findings of §3.1 for low  $Oh$  that the first impact peak amplitude  $F_1$  and the time to reach this peak amplitude  $t_1$  scale with  $F_\rho$  and  $\tau_\rho$ , respectively. As the Ohnesorge number increases further, the first impact force peak amplitude normalized with  $F_\rho$  begins to increase, indicating a transition around  $Oh \approx 0.1$ , where viscosity starts to play a significant role. At large  $Oh$ , we observe the scaling relationship (figure 5a)

$$F_1 \sim F_\rho \sqrt{Oh}. \quad (3.5)$$

The drop's momentum is still  $\rho_d V_0 D_0^3$  which must be balanced by the impulse from the substrate,  $F_1 t_1$  (see §3.1, [Gordillo et al. 2018](#), [Zhang et al. 2022](#), and figure 5b). Consequently, the time  $t_1$  follows

$$t_1 \sim \frac{\tau_\rho}{\sqrt{Oh}}. \quad (3.6)$$

Figure 5 further shows that these scaling laws are weakly dependent on the Weber number, as viscous dissipation consumes the entire initial kinetic energy of the impacting drop (figure 6). Once again, we stress that using the water-glycerol mixtures limits the range of  $Oh$  that we can probe experimentally. We further note that the first peak is robust and does not depend on the wettability of the substrate. Consequently, to compare with the existing data such as those in [Cheng et al. \(2022\)](#) with different liquids to cover a wider range of liquid viscosities and to account for the apparent  $We$ -dependence, we plot  $F_1$  compensated with  $F_\rho$  against the impact Reynolds number  $Re \equiv \sqrt{We/Oh} = V_0 D_0 / \nu_d$ . For the low  $Re$  regime, such a plot allows us to describe the  $We$  dependence on the prefactor more effectively, as illustrated in figure 5(c). However, it is important to note that some scatter is still observed at high  $Re$  values, which can be attributed to the  $We$  dependence of the impact force peak amplitude. This lack of a pure scaling behavior demonstrates how the interplay between kinetic energy and viscous dissipation within the drop dictates the functional dependence of the maximum impact force on  $Oh$ .

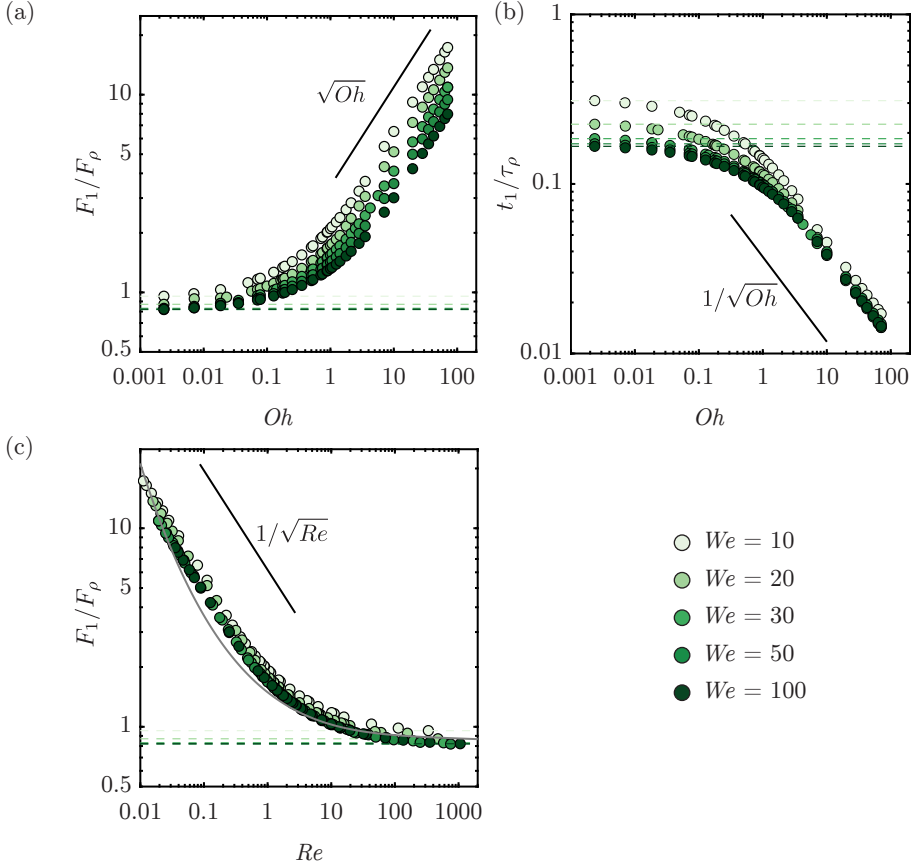


FIGURE 5. Anatomy of the first impact force peak amplitude for viscous impacts from our numerical simulations: the  $Oh$  dependence of (a) the magnitude  $F_1$  normalized by the inertial force scale  $\rho_d V_0^2 D_0^2$  and (b) the time  $t_1$  to reach the first force peak amplitude normalized by inertial timescale  $\tau_\rho = D_0/V_0$ . (c) The  $Re$  dependence of the magnitude  $F_1$  normalized by the inertial force scale  $\rho_d V_0^2 D_0^2$  as compared to the (implicit) theoretical calculation of Gordillo *et al.* (2018). The black line corresponds to the scaling relationship described in §3.2. The Weber number is color-coded.

269 To systematically elucidate these scaling behaviors in the limit of small  $Re$ , we need  
 270 to find the typical scales for the rate of change of kinetic energy and that of the rate of  
 271 viscous dissipation for the drop impact system. First, we can readily define an average  
 272 rate of viscous dissipation per unit mass as

$$\bar{\varepsilon} \sim \frac{1}{\tau_\rho} \frac{1}{D_0^3} \int_0^{\tau_\rho} \int_{\Omega} \nu_d (\mathcal{D} : \mathcal{D}) d\Omega dt, \quad (3.7)$$

273 where  $\nu_d$  is the kinematic viscosity of the drop and  $d\Omega$  is the volume element where  
 274 dissipation occurs. Notice that  $\bar{\varepsilon}$  has the dimensions of  $V_0^3/D_0$ , i.e., length squared over  
 275 time cubed or velocity squared over time, as it should be for dissipation rate of energy  
 276 per unit mass. We can estimate  $\Omega = D_{\text{foot}}^2 l_\nu$  (figure 6), where  $D_{\text{foot}}$  is the drop's foot  
 277 diameter in contact with the substrate and  $l_\nu$  is the viscous boundary layer thickness.  
 278 This boundary layer marks the region of strong velocity gradients ( $\sim V_0/l_\nu$ ) analogous to  
 279 the Mirels (1955) shockwave-induced boundary layer. For details, we refer the authors to

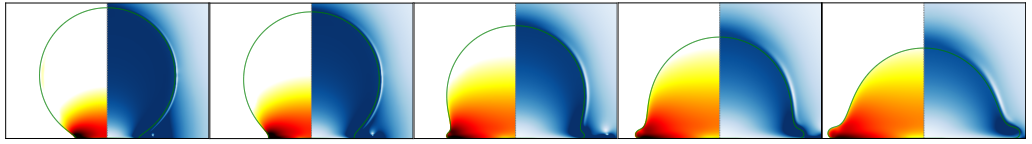
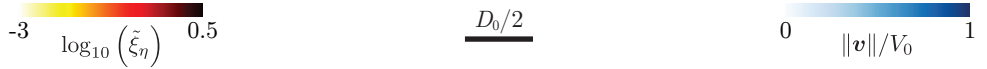
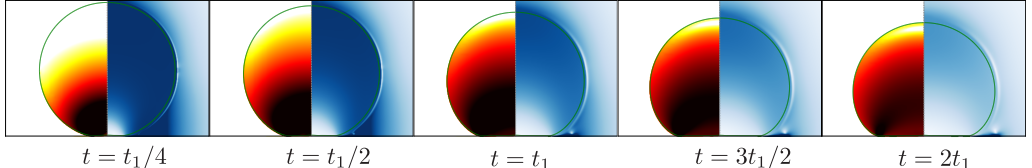
(a)  $Oh = 0.05$ (b)  $Oh = 0.5$ (c)  $Oh = 5$ 

FIGURE 6. Direct numerical simulations snapshots illustrating the drop impact dynamics for  $We = 100$  and  $Oh =$  (a) 0.05, (b) 0.5, and (c) 5. The left-hand side of each numerical snapshot shows the viscous dissipation function  $\xi_\eta$  normalized by the inertial scale  $\rho_d V_0^3 / D_0$ . The right-hand side shows the velocity field magnitude normalized by the impact velocity  $V_0$ .

280 Schlichting (1968); Schroll *et al.* (2010); Philippi *et al.* (2016). Consequently, the viscous  
281 dissipation rate scales as

$$\bar{\varepsilon} \sim \frac{1}{\tau_\rho D_0^3} \int_0^{\tau_\rho} \nu_d \left( \frac{V_0}{l_\nu} \right)^2 D_{\text{foot}}^2 l_\nu dt. \quad (3.8)$$

282 To calculate  $D_{\text{foot}}$ , we assume that the drop maintains a spherical cap shape throughout  
283 the impact (figure 6). To calculate the distance the drop would have traveled if there  
284 were no substrate, we use the relation  $d \sim V_0 t$ . Simple geometric arguments allow us  
285 to determine the relation between the foot diameter and this distance,  $D_{\text{foot}} \sim \sqrt{D_0 d}$   
286 (Lesser 1981; Mandre *et al.* 2009; Zheng *et al.* 2021; Bilotto *et al.* 2023; Bertin 2023).  
287 Interestingly, this scaling behavior is similar to the inertial limit (Wagner 1932; Bouwhuis  
288 *et al.* 2012; Philippi *et al.* 2016; Gordillo *et al.* 2019) as discussed by Langley *et al.* (2017);  
289 Bilotto *et al.* (2023). Furthermore, the viscous boundary layer  $l_\nu$  can be approximated  
290 using  $\sqrt{\nu_d t}$  (Mirels 1955; Eggers *et al.* 2010; Philippi *et al.* 2016). Filling these in (3.8),  
291 we get

$$\bar{\varepsilon} \sim \frac{1}{\tau_\rho D_0^2} \int_0^{\tau_\rho} \sqrt{\nu_d} V_0^3 \sqrt{t} dt, \quad (3.9)$$

292 which on integration gives

$$\bar{\varepsilon} \sim \sqrt{\nu_d \tau_\rho} V_0^3 / D_0^2, \quad (3.10)$$

293 where  $\tau_\rho$  is the inertial time scale. Here, we assume that for highly viscous drops, all

294 energy is dissipated within a fraction of  $\tau_\rho$ . Filling in (3.10) and normalizing  $\bar{\varepsilon}$  with the  
295 inertial scales  $V_0^3/D_0$ ,

$$\frac{\bar{\varepsilon}}{V_0^3/D_0} \sim \sqrt{\frac{\nu_d \tau_\rho}{D_0^2}} = \frac{1}{\sqrt{Re}} = \left( \frac{Oh}{\sqrt{We}} \right)^{1/2}. \quad (3.11)$$

296 Next, the kinetic energy of the falling drop is given by

$$\dot{K}(t) \equiv \frac{dK(t)}{dt} \sim \rho_d D_0^3 \bar{\varepsilon}, \quad \text{where } K(t) = \frac{1}{2} m (V(t))^2, \quad (3.12)$$

297 and  $V(t)$  is the drop's center of mass velocity. The left-hand side of (3.12) can be written  
298 as

$$\dot{K}(t) = m V(t) \frac{dV(t)}{dt} = F(t) V(t). \quad (3.13)$$

299 In equation (3.13),  $F(t)$  and  $V(t)$  scale with the first impact force peak amplitude  $F_1$   
300 and the impact velocity  $V_0$ , respectively, giving the typical scale of the rate of change of  
301 kinetic energy as

$$\dot{K}^* \sim F_1 V_0. \quad (3.14)$$

302 We stress that (3.14) states that the rate of change of kinetic energy is equal to the power  
303 of the normal reaction force, an observation already made by [Wagner \(1932\)](#) and [Philippi  
et al. \(2016\)](#) in the context of impact problems. Lastly, at large  $Oh$ , viscous dissipation  
304 enervates kinetic energy completely giving (figure 6c, also see: [Philippi et al. \(2016\)](#) and  
305 [Wildeman et al. \(2016\)](#)),  
306

$$\dot{K}^* \sim F_1 V_0 \sim \rho_d D_0^3 \bar{\varepsilon} \quad (3.15)$$

307 Additionally, we use the inertial scales to non-dimensionalize (3.15) and fill in (3.11),  
308 giving

$$\frac{F}{F_\rho} \sim \frac{\bar{\varepsilon}}{V_0^3/D_0} \sim \frac{1}{\sqrt{Re}} = \left( \frac{Oh}{\sqrt{We}} \right)^{1/2} \quad (3.16)$$

309 and using  $F_1 t_1 \sim \rho_d V_0 D_0^3 = F_\rho \tau_\rho$ ,

$$\frac{t_1}{\tau_\rho} \sim \left( \frac{\sqrt{We}}{Oh} \right)^{1/2}. \quad (3.17)$$

310 In summary, we use energy and momentum invariance to elucidate the parameter  
311 dependencies of the impact force as illustrated in figure 5. The scaling arguments  
312 capture the dominant force balance during the impact process, considering the relative  
313 importance of inertial, capillary, and viscous forces. As the dimensionless viscosity of  
314 impacting drops increases, the lack of surface deformation increases the normal reaction  
315 force (3.16). Further, the invariance of incoming drop momentum implies that this  
316 increase in normal reaction force occurs on a shorter timescale (3.17).

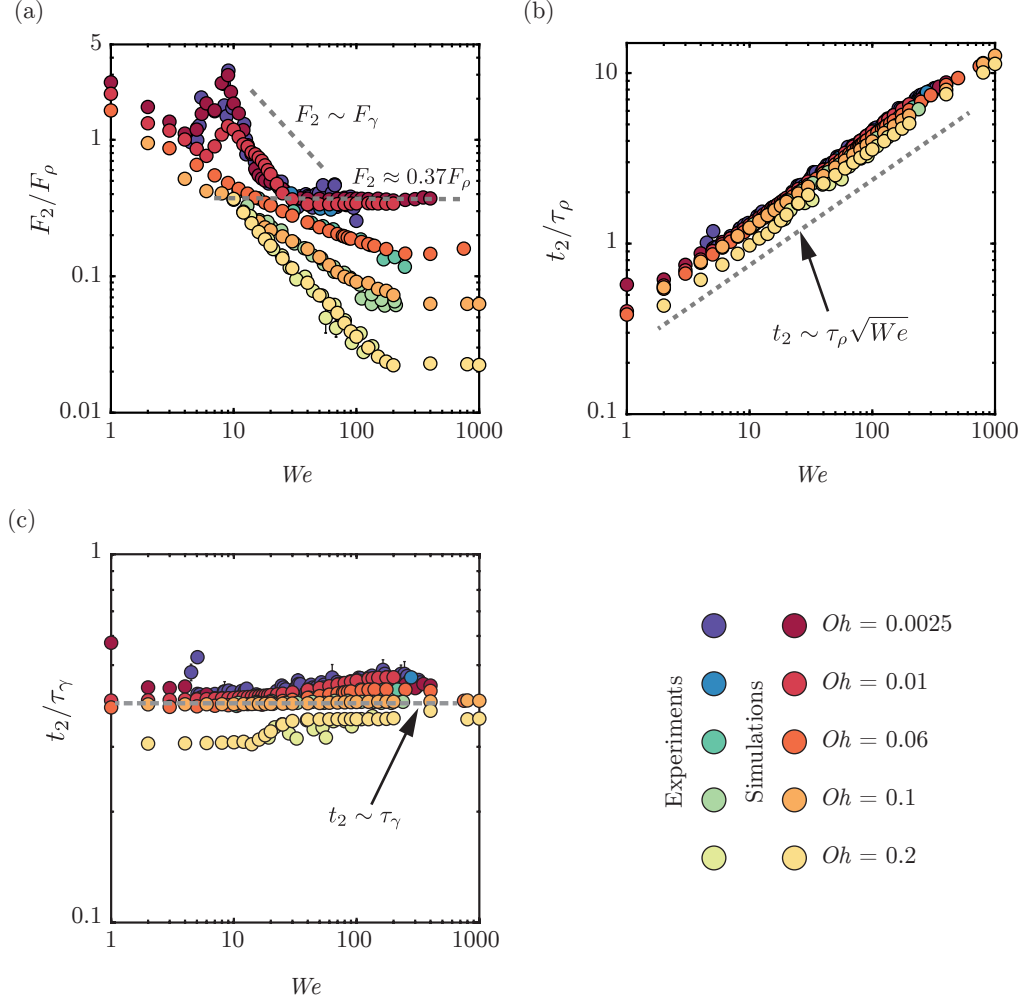


FIGURE 7. Anatomy of the second impact force peak amplitude:  $We$  dependence of the (a) magnitude  $F_2$  normalized by the inertial force scale  $F_\rho = \rho_d V_0^2 D_0^2$  and time  $t_2$  to reach the second force peak amplitude normalized by (b) the inertia-capillary time scale  $\tau_\gamma = \sqrt{\rho_d D_0^3 / \gamma}$  and (c) inertial timescale  $\tau_\rho = D_0 / V_0$ .

#### 317 4. Anatomy of the second impact force peak

318 This section delves into the anatomy of the second impact force peak amplitude  $F_2$  as a  
 319 function of the Weber  $We$  and Ohnesorge  $Oh$  numbers, summarized in figure 7. We once  
 320 again note the remarkable agreement between experiments and numerical simulations in  
 321 this figure.

322 Similar to the mechanism leading to the formation of the first peak (§3), also the  
 323 mechanism for the formation of this second peak is momentum conservation. As the  
 324 drop takes off the surface, it applies a force on the substrate. As noted in §1 and [Zhang et al. \(2022\)](#), this force also coincides with the formation of a Worthington jet (figure 2iv-vi). The time  $t_2$  at which the second peak is observed scales with the inertia-capillary  
 325 timescale and is insensitive to  $We$  and  $Oh$  (figure 7b,c). Once again, we invoke the analogy  
 326 between drop oscillation and drop impact to explain this behavior ([Richard et al. 2002](#);  
 327 [Lohse et al. 2005](#)).

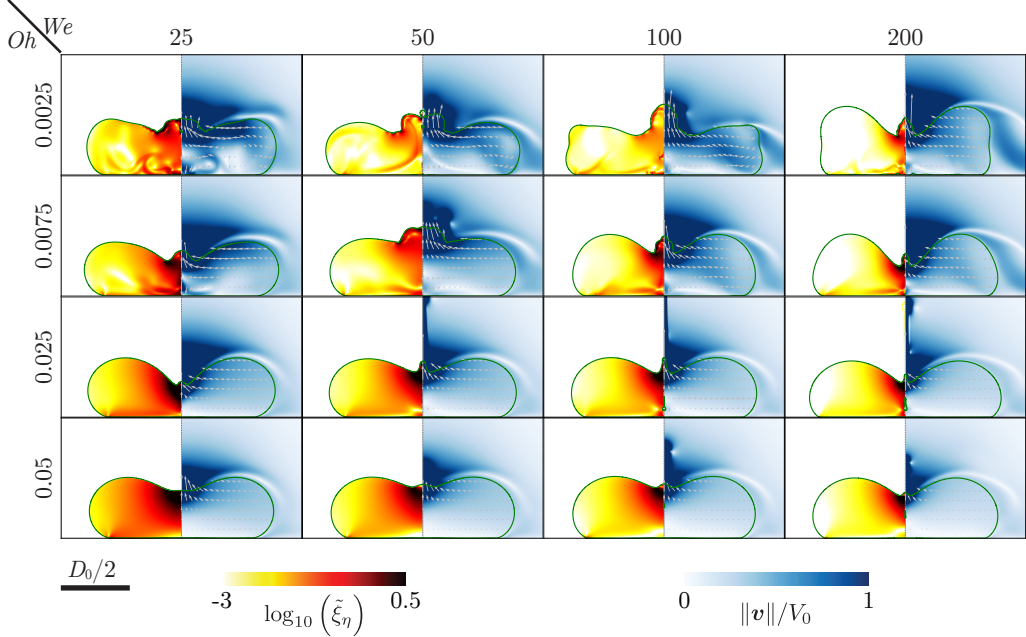


FIGURE 8. Direct numerical simulations snapshots illustrating the influence of  $We$  and  $Oh$  on the inception of the Worthington jet. All these snapshots are taken at the instant when the second peak appears in the temporal evolution of the normal reaction force ( $t = t_2$ ). The left-hand side of each numerical snapshot shows the viscous dissipation function  $\xi_\eta$  normalized by the inertial scale  $\rho_d V_0^3 / D_0$ . The right-hand side shows the velocity field magnitude normalized by the impact velocity  $V_0$ . The gray velocity vectors are plotted in the center of mass reference frame of the drop to clearly elucidate the internal flow.

329 Chevy *et al.* 2012). At the time instant  $t_2 \approx 0.44\tau_\gamma$ , the drop's internal motion undergoes  
 330 a transition from a predominantly radial flow to a vertical one due to the formation of  
 331 the Worthington jet (Chantelot 2018; Zhang *et al.* 2022). Figure 8 exemplifies this jet in  
 332 the  $Oh$ - $We$  parameter space, which is intricately related to the second peak in the drop  
 333 impact force. For low  $Oh$  and large  $We$ , the drop retraction follows a modified Taylor-  
 334 Culick dynamics (Bartolo *et al.* 2005; Eggers *et al.* 2010; Sanjay *et al.* 2022). As  $We$  is  
 335 increased, the jet gets thinner but faster, maintaining a constant momentum flux  $\rho_d V_j^2 d_j^2$ ,  
 336 where  $V_j$  and  $d_j$  are the jet's velocity and diameter, respectively (figure 8, Zhang *et al.*  
 337 2022). This invariance leads to the observed scaling  $F_2 \sim F_\rho$  in this regime ( $F_2 \approx 0.37F_\rho$   
 338 for  $We \geq 30, Oh \leq 0.01$ ).

339 Furthermore, the low  $We$  and  $Oh$  regime relies entirely on capillary pressure (figure 4).  
 340 Subsequently,  $F_2 \sim F_\gamma = \gamma D_0$  for  $Oh < 0.01$  and  $We < 30$  (figure 7). This flow focusing  
 341 (figure 8) is most efficient for  $We = 9$  (figure 9a,  $t_2/2 < t < t_2$ , Renardy *et al.* 2003;  
 342 Bartolo *et al.* 2006b) where the capillary resonance leads to a thin-fast jet, accompanied  
 343 by a bubble entrainment, reminiscent of the hydrodynamic singularity (figure 9, Zhang  
 344 *et al.* 2022; Sanjay *et al.* 2021). The characteristic feature of this converging flow is a  
 345 higher magnitude of  $F_2$  compared to  $F_1$  (figure 7).

346 However, this singular jet regime is very narrow in the  $Oh$ - $We$  phase space. Figure 9b  
 347 shows two cases for water drops ( $Oh = 0.0025$ ) at different  $We$  (5 and 12 for figures 9b-  
 348 i and b-ii, respectively). Bubble entrainment does not occur in either of these cases.  
 349 Consequently, the maximum force amplitude diminishes for these two cases (figure 7).  
 350 Nonetheless, these cases are still associated with high local viscous dissipation near the

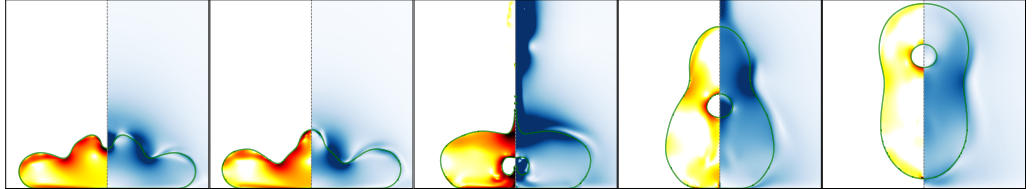
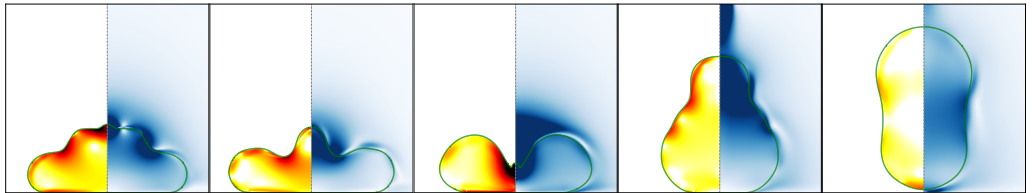
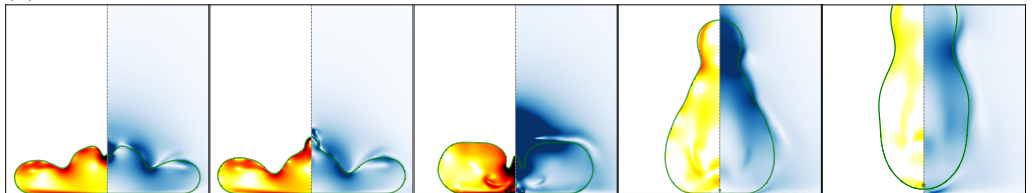
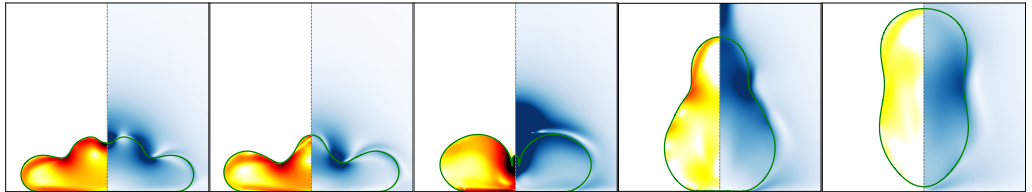
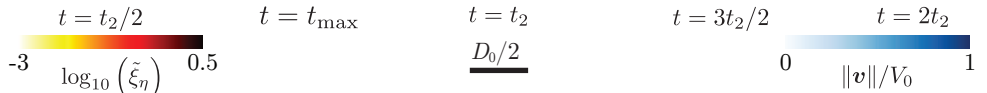
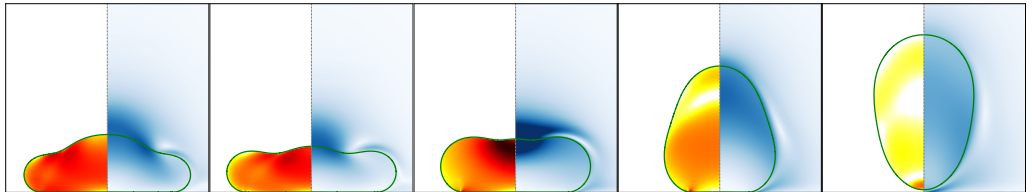
(a)  $We = 9, Oh = 0.0025$ (b)  $Oh = 0.0025$ (i)  $We = 5$ (ii)  $We = 12$ (c)  $We = 9$ (i)  $Oh = 0.005$ (ii)  $Oh = 0.05$ 

FIGURE 9. Direct numerical simulations snapshots illustrating the influence of  $We$  and  $Oh$  on the singular Worthington jet. (a)  $(We, Oh) = (9, 0.0025)$ , (b)  $Oh = 0.0025$  with  $We =$  (i) 5 and (ii) 12, and (c)  $We = 9$  with  $Oh =$  (i) 0.005 and (ii)  $Oh = 0.05$ . The left-hand side of each numerical snapshot shows the viscous dissipation function  $\xi_\eta$  normalized by inertial scale  $\rho_d V_0^3 / D_0$ . The right-hand side shows the velocity field magnitude normalized by the impact velocity  $V_0$ .

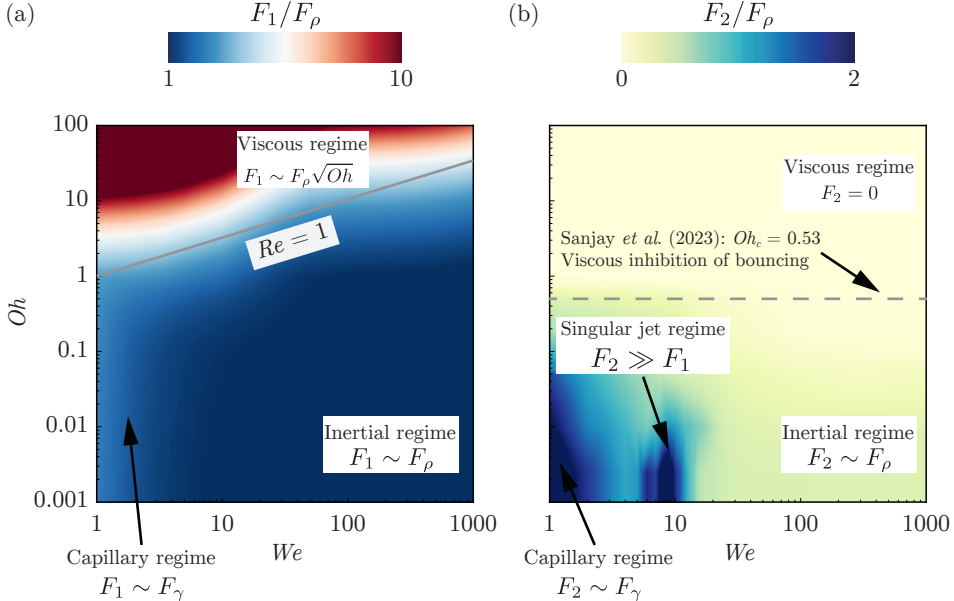


FIGURE 10. Regime map in terms of the drop Ohnesorge number  $Oh$  and the impact Weber number  $We$  to summarize the two peaks in the impact force by showing the different regimes described in this work based on (a) the first peak in the impact force peak amplitude  $F_1$  and (b) the second peak in the impact force peak amplitude  $F_2$ . Both peaks are normalized by the inertial force scale  $F_\rho = \rho_d V_0^2 D_0^2$ . These regime maps are constructed using  $\sim 1500$  simulations in the range  $0.001 \leq Oh \leq 100$  and  $1 \leq We \leq 1000$ . The gray solid line in (a) and dashed line in (b) mark the inertial-viscous transition ( $Re = 1$ ) and the bouncing-no-bouncing transition ( $Oh_c = 0.53$  for  $Bo = 1$ , see [Sanjay et al. \(2023a\)](#)), respectively.

axis of symmetry owing to the singular nature of the flow. Another mechanism to inhibit this singular Worthington jet is viscous dissipation in the bulk. As the Ohnesorge number increases, this singular jet formation disappears ( $Oh = 0.005$ , figure 9c-i), significantly reducing the second peak of the impact force. For even higher viscosities, the drop no longer exhibits the sharp, focused jet formation seen at lower viscosities, and the second peak in the force is notably diminished ( $Oh = 0.05$ , figure 9c-ii).

Lastly, as  $Oh$  increases, bulk dissipation becomes dominant (apparent from increasing  $Oh$  at fixed  $We$  in figure 8) and can entirely inhibit drop bouncing. Recently, [Jha et al. \(2020\)](#); [Sanjay et al. \(2023a\)](#) showed that there exists a critical  $Oh$ , two orders of magnitude higher than that of a 2 mm diameter water drop, beyond which drops do not bounce either, irrespective of their impact velocity. Consequently, the second peak in the impact force diminishes for larger  $Oh$ , which explains the monotonic decrease of the amplitude  $F_2$  observed in figure 7 for  $We > 30, Oh > 0.01$ .

## 5. Conclusion and outlook

In this work, we study the forces and dissipation encountered during the drop impact process by employing experiments, numerical simulations, and theoretical scaling laws. We vary the two dimensionless control parameters—the Weber ( $We$ : dimensionless impact kinetic energy) and the Ohnesorge number ( $Oh$ : dimensionless viscosity) independently to elucidate the intricate interplay between inertia, viscosity, and surface tension in governing the forces exerted by a liquid drop upon impact on a non-wetting substrate.

For the first impact force peak amplitude  $F_1$ , owing to the momentum balance after

372 the inertial shock at impact, figure 10(a) summarizes the different regimes in the  $Oh$ - $We$   
 373 phase space. For low  $Oh$ , inertial forces predominantly dictate the impact dynamics, such  
 374 that  $F_1$  scales with the inertial force  $F_\rho$  (Philippi *et al.* 2016; Gordillo *et al.* 2018; Mitchell  
 375 *et al.* 2019; Cheng *et al.* 2022; Zhang *et al.* 2022) and is insensitive to viscosity variations  
 376 up to 100-fold. As  $Oh$  increases, the viscosity becomes significant, leading to a new scaling  
 377 law:  $F_1 \sim F_\rho \sqrt{Oh}$ . The paper unravels this viscous scaling behavior by accounting for  
 378 the loss of initial kinetic energy owing to viscous dissipation inside the drop. Lastly, at  
 379 low  $We$ , the capillary pressure inside the drop leads to the scaling  $F_1 \sim F_\gamma$  (Moláček &  
 380 Bush 2012; Chevy *et al.* 2012).

381 The normal reaction force described in this work is responsible for deforming the  
 382 drop as it spreads onto the substrate, where it stops thanks to surface tension. If the  
 383 substrate is non-wetting, it retracts to minimize the surface energy and finally takes off  
 384 (Richard & Quéré 2000). In this case, the momentum conservation leads to the formation  
 385 of a Worthington jet and a second peak in the normal reaction force, as summarized in  
 386 figure 10(b). For low  $Oh$  and high  $We$ , the second force peak amplitude scales with the  
 387 inertial force ( $F_\rho$ ), following a modified Taylor-Culick dynamics (Eggers *et al.* 2010). In  
 388 contrast, capillary forces dominate at low  $We$  and low  $Oh$ , leading to a force amplitude  
 389 scaling of  $F_2 \sim F_\gamma$ . We also identify a narrow regime in the  $Oh$ - $We$  phase space where a  
 390 singular Worthington jet forms, significantly increasing  $F_2$  (Bartolo *et al.* 2006b; Zhang  
 391 *et al.* 2022), localized in the parameter space for  $We \approx 9$  and  $Oh < 0.01$ . As  $Oh$  increases,  
 392 bulk viscous dissipation counteracts this jet formation, diminishing the second peak and  
 393 ultimately inhibiting drop bouncing.

394 Our findings have far-reaching implications, not only enriching the fundamental  
 395 understanding of fluid dynamics of drop impact but also informing practical applications  
 396 in diverse fields such as inkjet printing, public health, agriculture, and material science  
 397 where the entire range of  $Oh$ - $We$  phase space is relevant (figures 1b and 10). While this  
 398 has identified new scaling laws, it also opens avenues for future research. For instance,  
 399 it would be interesting to use the energy accounting approach to unify the scaling laws  
 400 for the maximum spreading diameter for arbitrary  $Oh$  (Laan *et al.* 2014; Wildeman  
 401 *et al.* 2016). Although, the implicit theoretical model summarized in Cheng *et al.* (2022)  
 402 describes most of data in figure 5, we stress the importance of having a predictive model  
 403 to determine  $F_1$  for given  $We$  and  $Oh$  (Sanjay & Lohse 2024). The  $We$  influence on  
 404 the impact force also warrants further exploration, especially in the regime  $We \ll 1$  for  
 405 arbitrary  $Oh$  (Chevy *et al.* 2012; Moláček & Bush 2012) and drop impact on compliant  
 406 surfaces (Alventosa *et al.* 2023b; Ma & Huang 2023). Another potential extension of this  
 407 work is to non-Newtonian fluids (Martouzet *et al.* 2021; Agüero *et al.* 2022; Bertin 2023;  
 408 Jin *et al.* 2023).

409  
 410 **Code availability.** The codes used in the present article, and the parameters and data  
 411 to reproduce figures 3 and 7 are permanently available at [Sanjay \(2024\)](#).

412  
 413 **Acknowledgements.** We would like to thank Vincent Bertin for comments on the  
 414 manuscript. We would also like to thank Andrea Prosperetti, Pierre Chantelot, Devaraj  
 415 van der Meer, and Uddalok Sen for illuminating discussions.

416  
 417 **Funding.** We acknowledge the funding by the ERC Advanced Grant No. 740479-DDD  
 418 and NWO-Canon grant FIP-II. B.Z and C.L are grateful for the support from National  
 419 Natural Science Foundation of China (Grant No. 12172189, 11921002, 11902179). This

420 work was carried out on the national e-infrastructure of SURFsara, a subsidiary of SURF  
421 cooperation, the collaborative ICT organization for Dutch education and research. This  
422 work was sponsored by NWO - Domain Science for the use of supercomputer facilities.

423  
424 **Declaration of Interests.** The authors report no conflict of interest.

425  
426 **Authors' ORCID.**

427 V. Sanjay <https://orcid.org/0000-0002-4293-6099>;  
428 B. Zhang <https://orcid.org/0000-0001-8550-2584>;  
429 C. Lv <https://orcid.org/0000-0001-8016-6462>;  
430 D. Lohse <https://orcid.org/0000-0003-4138-2255>.

431  
432 **Appendix A. Note on the error characterization for the control  
433 parameters**

434 This appendix outlines the methodology for characterizing experimental errors in  
435 quantification of the drop's size and impact velocities which is crucial for accurate  
436 calculation of the dimensionless control parameters  $We$  and  $Oh$ . The drop diameter  
437 determination involves multiple steps. First, we measure the total mass ( $M_{100}$ ) of 100  
438 drops using an electric balance. From this mass, using the liquid density and assuming  
439 spherical shape, we calculated the drop diameter ( $D_0$ ). We repeated this process five  
440 times, yielding  $D_{0,1}$  through  $D_{0,5}$ . The average of these measurements provided the  
441 final drop diameter ( $D_0$ ) and its standard error. For impact velocity determination, we  
442 extracted data from experimental high-speed imagery. By tracking the drop center's  
443 position in successive frames prior to substrate contact, and knowing the frame rate, we  
444 calculated the impact velocity. We repeated this process for five trials, obtaining  $V_{0,1}$   
445 through  $V_{0,5}$ . The average of these values gave the final impact velocity ( $V_0$ ) and its  
446 standard error.

447 The standard errors for drop diameters do not exceed 0.13 mm. For instance, drops  
448 with Ohnesorge numbers of 0.0025, 0.06, and 0.2 have diameters of  $2.05 \pm 0.13$  mm,  $2.52 \pm$   
449 0.11 mm, and  $2.54 \pm 0.09$  mm, respectively. The standard errors for impact velocities did  
450 not exceed 0.02 m/s. For the same  $Oh$  values, the impact velocities were  $1.2 \pm 0.002$  m/s,  
451  $0.97 \pm 0.01$  m/s, and  $0.96 \pm 0.01$  m/s, respectively. The combined errors in  $D_0$  and  $V_0$   
452 resulted in approximately  $\pm 7\%$  error in Weber number  $We$  and  $\pm 3\%$  error in Ohnesorge  
453 number  $Oh$ . Consequently, the horizontal error bars, which relate to errors in the control  
454 parameters, are smaller than the symbol sizes in our figures.

455  
456 **Appendix B. Role of gravity on drop impact forces**

457 Following table 1 and considering the variation in impacting drop diameter (appendix A),  
458 the Bond number (equation (1.3)) in our experiments ranges from 0.5 to 1.25,  
459 introducing an additional dimensionless control parameter alongside  $We$  and  $Oh$ . Gravity  
460 typically plays a negligible role in these impact processes (Sanjay et al. 2023a; Sanjay &  
461 Lohse 2024). We undertook a sensitivity test varying the Bond number from 0 to 1.25 in  
462 our simulations. Figure A 1 confirms the leading-order Bond invariance of the results as  
463 the impact force profiles, including both force peaks  $F_1$  and  $F_2$  and their corresponding  
464 times  $t_1$  and  $t_2$ , remain invariant to these Bond number variations. Notably, while gravity  
465 does play a role in drop impact dynamics, particularly for longer time scales and in  
determining the critical Ohnesorge number  $Oh_c$  for bouncing inhibition (see figure 10b)

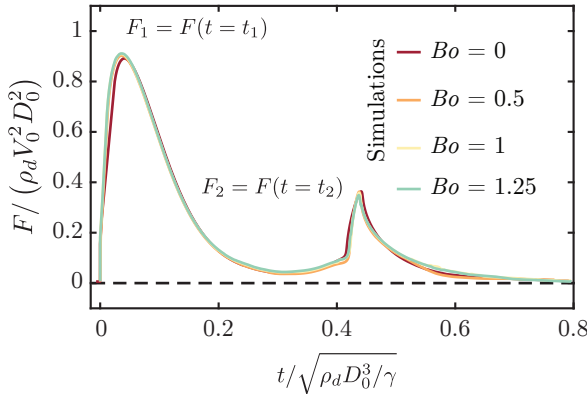


FIGURE A 1. Comparison of the drop impact force  $F(t)$  obtained from simulations for the four different Bond numbers  $Bo = 0, 0.5, 1, 1.25$ . Here,  $Oh = 0.06$  and  $We = 40$ . Both force peaks  $F_1$  and  $F_2$  as well as time to reach these peaks  $t_1$  and  $t_2$  are invariant to variation in  $Bo$ .

and Sanjay *et al.* (2023a)), its effect on the initial impact force peaks is minimal for the parameter range studied here (large Froude numbers,  $Fr > 1$ ). This Bond number invariance allows us to focus on the more dominant effects of Weber and Ohnesorge numbers. Consequently, we selected the representative value of  $Bo = 1$ , corresponding to a diameter of 0.00254 mm, density 1000 kg/m<sup>3</sup>, gravitational acceleration 10 m/s<sup>2</sup>, and surface tension 0.061 N/m.

## REFERENCES

- AGÜERO, E. A., ALVENTOSA, L. F. L., HARRIS, D. M. & GALEANO-RIOS, C. A. 2022 Impact of a rigid sphere onto an elastic membrane. *Proc. R. Soc. Lond. A* **478** (2266), 20220340.
- AHMAD, M., SCHATZ, M. & CASEY, M. V. 2013 Experimental investigation of droplet size influence on low pressure steam turbine blade erosion. *Wear* **303**, 83–86.
- ALVENTOSA, L. F. L., CIMPEANU, R. & HARRIS, D. M. 2023a Inertio-capillary rebound of a droplet impacting a fluid bath. *J. Fluid Mech.* **958**, A24.
- ALVENTOSA, L. F. L., CIMPEANU, R. & HARRIS, D. M. 2023b Inertio-capillary rebound of a droplet impacting a fluid bath. *J. Fluid Mech.* **958**, A24.
- AMIRZADEH, B., LOUGHALAM, A., RAESSI, M. & TOOKABONI, M. 2017 A computational framework for the analysis of rain-induced erosion in wind turbine blades. *J. Wind Eng. Ind. Aerodyn.* **163**, 33–43.
- BARTOLO, D., BOUAMRIRENE, F., VERNEUIL, E., BUGUIN, A., SILBERZAN, P. & MOULINET, S. 2006a Bouncing or sticky droplets: Impalement transitions on superhydrophobic micropatterned surfaces. *Europhys. Lett.* **74** (2), 299.
- BARTOLO, D., BOUDAOUED, A., NARCY, G. & BONN, D. 2007 Dynamics of non-Newtonian droplets. *Phys. Rev. Lett.* **99** (17), 174502.
- BARTOLO, D., JOSSERAND, C. & BONN, D. 2005 Retraction dynamics of aqueous drops upon impact on non-wetting surfaces. *J. Fluid Mech.* **545**, 329–338.
- BARTOLO, D., JOSSERAND, C. & BONN, D. 2006b Singular jets and bubbles in drop impact. *Phys. Rev. Lett.* **96** (12), 124501.
- BERGERON, V., BONN, D., MARTIN, J. Y. & VOVELLE, L. 2000 Controlling droplet deposition with polymer additives. *Nature* **405** (6788), 772–775.
- BERNY, A., POPINET, S., SÉON, T. & DEIKE, L. 2021 Statistics of jet drop production. *Geophys. Res. Lett.* **48** (10), e2021GL092919.
- BERTIN, V. 2023 Similarity solutions in elastohydrodynamic bouncing. *J. Fluid Mech.* **986**.
- BIANCE, A.-L., CHEVY, F., CLANET, C., LAGUBEAU, G. & QUÉRÉ, D. 2006 On the elasticity of an inertial liquid shock. *J. Fluid Mech.* **554**, 47–66.
- BIOLTO, J., KOLINSKI, J. M., LECAMPION, B., MOLINARI, J.-F., SUBHASH, G. & GARCIA-

- SUAREZ, J. 2023 Fluid-mediated impact of soft solids. *arXiv preprint arXiv:2311.09953*
- BONN, D., EGGERS, J., INDEKEU, J., MEUNIER, J. & ROLLEY, E. 2009 Wetting and spreading. *Rev. Mod. Phys.* **81** (2), 739–805.
- BORMASHENKO, E., POGREB, R., WHYMAN, G. & ERLICH, M. 2007 Resonance Cassie-Wenzel wetting transition for horizontally vibrated drops deposited on a rough surface. *Langmuir* **23** (24), 12217–12221.
- BOUROUIBA, L. 2021 The fluid dynamics of disease transmission. *Annu. Rev. Fluid Mech.* **53**, 473–508.
- BOUWHUIS, W., VAN DER VEEN, R. C. A., TRAN, T., KEIJ, D. L., WINKELS, K. G., PETERS, I. R., VAN DER MEER, D., SUN, C., SNOEIJER, J. H. & LOHSE, D. 2012 Maximal air bubble entrainment at liquid-drop impact. *Phys. Rev. Lett.* **109** (26), 264501.
- BRACKBILL, J. U., KOTHE, D. B. & ZEMACH, C. 1992 A continuum method for modeling surface tension. *J. Comput. Phys.* **100** (2), 335–354.
- CALLIES, M. & QUÉRÉ, D. 2005 On water repellency. *Soft Matter* **1** (1), 55–61.
- CHANTELOT, P. 2018 Rebonds spéciaux de liquides. PhD thesis, Université Paris-Saclay (ComUE).
- CHEN, X., MA, R., LI, J., HAO, C., GUO, W., LUK, B. L., LI, S. C., YAO, S. & WANG, Z. 2012 Evaporation of droplets on superhydrophobic surfaces: surface roughness and small droplet size effects. *Phys. Rev. Lett.* **109** (11), 116101.
- CHENG, N.-S. 2008 Formula for the viscosity of a glycerol–water mixture. *Ind. Eng. Chem. Res.* **47** (9), 3285–3288.
- CHENG, X., SUN, T.-P. & GORDILLO, L. 2022 Drop impact dynamics: impact force and stress distributions. *Annu. Rev. Fluid Mech.* **54**, 57–81.
- CHEVY, F., CHEPELIANSKII, A., QUÉRÉ, D. & RAPHAËL, E. 2012 Liquid Hertz contact: softness of weakly deformed drops on non-wetting substrates. *Europhys. Lett.* **100** (5), 54002.
- CHO, H. J., PRESTON, D. J., ZHU, Y. & WANG, E. N. 2016 Nanoengineered materials for liquid–vapour phase-change heat transfer. *Nat. Rev. Mater.* **2** (2), 16092.
- CHUBYNSKY, M. V., BELOUSOV, K. I., LOCKERBY, D. A. & SPRITTLES, J. E. 2020 Bouncing off the walls: the influence of gas-kinetic and van der Waals effects in drop impact. *Phys. Rev. Lett.* **124**, 084501.
- CLANET, C., BÉGUIN, C., RICHARD, D. & QUÉRÉ, D. 2004 Maximal deformation of an impacting drop. *J. Fluid Mech.* **517**, 199–208.
- DA VINCI, L. 1508 *Codex Hammer* (earlier *Codex Leicester*). In *The Notebooks of Leonardo da Vinci* (ed. and trans. E. MacCurdy).. George Braziller.
- DE GENNES, P. G. 1985 Wetting: statics and dynamics. *Rev. Mod. Phys.* **57**, 827–863.
- DENG, X., MAMMEN, L., BUTT, H.-J. & VOLLMER, D. 2012 Candle soot as a template for a transparent robust superamphiphobic coating. *Science* **335** (6064), 67–70.
- DRISCOLL, M. M. & NAGEL, S. R. 2011 Ultrafast interference imaging of air in splashing dynamics. *Phys. Rev. Lett.* **107** (15), 154502.
- EGGERS, J., FONTELOS, M. A., JOSSERAND, C. & ZALESKI, S. 2010 Drop dynamics after impact on a solid wall: theory and simulations. *Phys. Fluids* **22** (6), 062101.
- FUKAI, J., SHIIBA, Y., YAMAMOTO, T., MIYATAKE, O., POULIKAKOS, D., MEGARIDIS, C. M. & ZHAO, Z. 1995 Wetting effects on the spreading of a liquid droplet colliding with a flat surface: experiment and modeling. *Phys. Fluids* **7**, 236–247.
- GARCÍA-GEIJO, P., RIBOUX, G & GORDILLO, JM 2024 The skating of drops impacting over gas or vapour layers. *J. Fluid Mech.* **980**, A35.
- GAUTHIER, A., SYMON, S., CLANET, C. & QUÉRÉ, D. 2015 Water impacting on superhydrophobic macrotextures. *Nat. Commun.* **6** (1), 1–6.
- GOHARDANI, O. 2011 Impact of erosion testing aspects on current and future flight conditions. *Prog. Aerosp. Sci.* **47** (4), 280–303.
- GORDILLO, J. M., RIBOUX, G. & QUINTERO, E. S. 2019 A theory on the spreading of impacting droplets. *J. Fluid Mech.* **866**, 298–315.
- GORDILLO, L., SUN, T.-P. & CHENG, X. 2018 Dynamics of drop impact on solid surfaces: evolution of impact force and self-similar spreading. *J. Fluid Mech.* **840**, 190–214.
- GORIN, B., DI MAURO, G., BONN, D. & KELLAY, H. 2022 Universal aspects of droplet spreading dynamics in Newtonian and non-Newtonian fluids. *Langmuir* **38** (8), 2608–2613.

- 557 HAO, C., LIU, Y., CHEN, X., LI, J., ZHANG, M., ZHAO, Y. & WANG, Z. 2016 Bioinspired  
558 interfacial materials with enhanced drop mobility: from fundamentals to multifunctional  
559 applications. *Small* **12** (14), 1825–1839.
- 560 HE, L., DING, L., LI, B., MU, W., LI, P. & LIU, F. 2021 Optimization strategy to  
561 inhibit droplets rebound on pathogen-modified hydrophobic surfaces. *ACS Appl. Mater.  
562 Interfaces* **13** (32), 38018–38028.
- 563 HOFFMAN, H., SIJS, R., DE GOEDE, T. & BONN, D. 2021 Controlling droplet deposition with  
564 surfactants. *Phys. Rev. Fluids* **6** (3), 033601.
- 565 JHA, A., CHANTELOT, P., CLANET, C. & QUÉRÉ, D. 2020 Viscous bouncing. *Soft Matter* **16**,  
566 7270–7273.
- 567 JI, B., YANG, Z. & FENG, J. 2021 Compound jetting from bubble bursting at an air-oil-water  
568 interface. *Nat. Commun.* **12** (1), 6305.
- 569 JIN, P., ZHAO, K., BLIN, Z., ALLAIS, M., MOUTERDE, T. & QUÉRÉ, D. 2023 When marbles  
570 challenge pearls. *J. Chem. Phys.* **158** (20).
- 571 JOSSERAND, C. & THORODDSEN, S. T. 2016 Drop impact on a solid surface. *Annu. Rev. Fluid  
572 Mech.* **48**, 365–391.
- 573 JOWKAR, S. & MORAD, M. R. 2019 Rebounding suppression of droplet impact on hot surfaces:  
574 effect of surface temperature and concaveness. *Soft Matter* **15** (5), 1017–1026.
- 575 KIM, J. 2007 Spray cooling heat transfer: The state of the art. *Int. J. Heat Fluid Flow* **28** (4),  
576 753–767.
- 577 KIM, S., WU, Z., ESMAILI, E., DOMBROSKIE, J. J & JUNG, S. 2020 How a raindrop gets  
578 shattered on biological surfaces. *Proc. Natl. Acad. Sci. U.S.A.* **117** (25), 13901–13907.
- 579 KOLINSKI, J. M., MAHADEVAN, L. & RUBINSTEIN, S. M. 2014 Drops can bounce from perfectly  
580 hydrophilic surfaces. *Europhys. Lett.* **108**, 24001.
- 581 KOOIJ, S., SIJS, R., DENN, M. M., VILLERMAUX, E. & BONN, D. 2018 What determines the  
582 drop size in sprays? *Phys. Rev. X* **8** (3), 031019.
- 583 LAAN, N., DE BRUIN, K. G., BARTOLO, D., JOSSERAND, C. & BONN, D. 2014 Maximum  
584 diameter of impacting liquid droplets. *Phys. Rev. Appl.* **2** (4), 044018.
- 585 LAFUMA, A. & QUÉRÉ, D. 2003 Superhydrophobic states. *Nat. Mater.* **2** (7), 457–460.
- 586 LANGLEY, K., LI, E. Q. & THORODDSEN, S. T. 2017 Impact of ultra-viscous drops: air-film  
587 gliding and extreme wetting. *J. Fluid Mech.* **813**, 647–666.
- 588 LESSER, M. B. 1981 Analytic solution of liquid-drop impact problems. *Proc. R. Soc. Lond. A*  
589 **377** (1770), 289–308.
- 590 LI, J., ZHANG, B., GUO, P. & LV, Q. 2014 Impact force of a low speed water droplet colliding  
591 on a solid surface. *J. Appl. Phys.* **116** (21), 214903.
- 592 LI, Y., QUÉRÉ, D., LV, C. & ZHENG, Q. 2017 Monostable superrepellent materials. *Proc. Natl  
593 Acad. Sci. USA* **114** (13), 3387–3392.
- 594 LIU, M., WANG, S. & JIANG, L. 2017 Nature-inspired superwettability systems. *Nat. Rev.  
595 Mater.* **2** (7), 17036.
- 596 LOHSE, D. 2022 Fundamental fluid dynamics challenges in inkjet printing. *Annu. Rev. Fluid  
597 Mech.* **54**, 349–382.
- 598 LOHSE, D. & VILLERMAUX, E. 2020 Double threshold behavior for breakup of liquid sheets.  
599 *Proc. Natl. Acad. Sci. U.S.A.* **117**, 18912–18914.
- 600 MA, Y. & HUANG, H. 2023 Scaling maximum spreading of droplet impacting on flexible  
601 substrates. *J. Fluid Mech.* **958**, A35.
- 602 MANDRE, S., MANI, M. & BRENNER, M. P. 2009 Precursors to splashing of liquid droplets on  
603 a solid surface. *Phys. Rev. Lett.* **102** (13), 134502.
- 604 MARTOUZET, G., JØRGENSEN, L., PELET, Y., BIANCE, A.-L. & BARENTIN, C. 2021 Dynamic  
605 arrest during the spreading of a yield stress fluid drop. *Phys. Rev. Fluids* **6** (4), 044006.
- 606 MIRELS, H. 1955 Laminar boundary layer behind shock advancing into stationary fluid. *NACA  
607 TN* **3401**, 25.
- 608 MITCHELL, B. R., KLEWICKI, J. C., KORKOLIS, Y. P. & KINSEY, B. L. 2019 The transient  
609 force profile of low-speed droplet impact: measurements and model. *J. Fluid Mech.* **867**,  
610 300–322.
- 611 MOLÁČEK, J. & BUSH, J. W. M. 2012 A quasi-static model of drop impact. *Phys. Fluids*  
612 **24** (12), 127103.

- NEARING, M. A., BRADFORD, J. M. & HOLTZ, R. D. 1986 Measurement of force vs. time relations for waterdrop impact. *Soil Sci. Soc. Am. J.* **50**, 1532–1536.
- PAPADOPOULOS, P., MAMMEN, L., DENG, X., VOLLMER, D. & BUTT, H.-J. 2013 How superhydrophobicity breaks down. *Proc. Natl Acad. Sci. USA* **110** (9), 3254–3258.
- PHILIPPI, J., LAGRÉE, P.-Y. & ANTKOWIAK, A. 2016 Drop impact on a solid surface: short-time self-similarity. *J. Fluid Mech.* **795**, 96–135.
- PÖHLKER, M. L., PÖHLKER, C., KRÜGER, O. O., FÖRSTER, J.-D., BERKEMEIER, T., ELBERT, W., FRÖHLICH-NOWOISKY, J., PÖSCHL, U., BAGHERI, G., BODENSCHATZ, E., HUFFMAN, J. A., SCHEITHAUER, S. & MIKHAILOV, E. 2023 Respiratory aerosols and droplets in the transmission of infectious diseases. *Rev. Mod. Phys.* **95** (4), 045001.
- POPINET, S. 2009 An accurate adaptive solver for surface-tension-driven interfacial flows. *J. Comput. Phys.* **228** (16), 5838–5866.
- POPINET, S. 2018 Numerical models of surface tension. *Annu. Rev. Fluid Mech.* **50**, 49–75.
- POPINET, S. & COLLABORATORS 2013–2023 Basilisk C: volume of fluid method. <http://basilisk.fr> (Last accessed: August 23, 2023).
- QUÉRÉ, D. 2008 Wetting and roughness. *Annu. Rev. Mater. Res.* **38**, 71–99.
- RAMÍREZ-SOTO, O., SANJAY, V., LOHSE, D., PHAM, J. T. & VOLLMER, D. 2020 Lifting a sessile drop from a superamphiphobic surface with an impacting one. *Sci. Adv.* **6**, eaba4330.
- REIN, M. 1993 Phenomena of liquid drop impact on solid and liquid surfaces. *Fluid Dyn. Res.* **12**, 61–93.
- RENARDY, Y., POPINET, S., DUCHEMIN, L., RENARDY, M., ZALESKI, S., JOSSERAND, C., DRUMRIGHT-CLARKE, M. A., RICHARD, D., CLANET, C. & QUÉRÉ, D. 2003 Pyramidal and toroidal water drops after impact on a solid surface. *J. Fluid Mech.* **484**, 69–83.
- RIBOUX, G. & GORDILLO, J. M. 2014 Experiments of drops impacting a smooth solid surface: a model of the critical impact speed for drop splashing. *Phys. Rev. Lett.* **113** (2), 024507.
- RICHARD, D., CLANET, C. & QUÉRÉ, D. 2002 Contact time of a bouncing drop. *Nature* **417** (6891), 811–811.
- RICHARD, D. & QUÉRÉ, D. 2000 Bouncing water drops. *Europhys. Lett.* **50** (6), 769–775.
- SANJAY, V. 2022 Viscous Free-Surface Flows. PhD thesis, University of Twente.
- SANJAY, V. 2024 Code repository: The role of viscosity on drop impact forces. <https://zenodo.org/doi/10.5281/zenodo.13381995> (Last accessed: Aug 28, 2024).
- SANJAY, V., CHANTELOT, P. & LOHSE, D. 2023a When does an impacting drop stop bouncing? *Journal of Fluid Mechanics* **958**, A26.
- SANJAY, V., LAKSHMAN, S., CHANTELOT, P., SNOEIJER, J. H. & LOHSE, D. 2023b Drop impact on viscous liquid films. *J. Fluid Mech.* **958**, A25.
- SANJAY, V. & LOHSE, D. 2024 Unifying theory of scaling in drop impact: Forces & maximum spreading diameter. *arXiv preprint arXiv: 2408.12714*.
- SANJAY, V., LOHSE, D. & JALAAL, M. 2021 Bursting bubble in a viscoplastic medium. *J. Fluid Mech.* **922**, A2.
- SANJAY, V., SEN, U., KANT, P. & LOHSE, D. 2022 Taylor-Culick retractions and the influence of the surroundings. *J. Fluid Mech.* **948**, A14.
- SBRAGAGLIA, M., PETERS, A. M., PIRAT, C., BORKENT, B. M., LAMMERTINK, R. G. H., WESSLING, M. & LOHSE, D. 2007 Spontaneous breakdown of superhydrophobicity. *Phys. Rev. Lett.* **99** (15), 156001.
- SCHLICHTING, H. 1968 *Boundary-layer theory*. McGraw-Hill.
- SCHROLL, R. D., JOSSERAND, C., ZALESKI, S. & ZHANG, W. W. 2010 Impact of a viscous liquid drop. *Phys. Rev. Lett.* **104** (3), 034504.
- SHARMA, P. K. & DIXIT, H. N. 2021 Regimes of wettability-dependent and wettability-independent bouncing of a drop on a solid surface. *J. Fluid Mech.* **908**, A37.
- SHIRI, S. & BIRD, J. C. 2017 Heat exchange between a bouncing drop and a superhydrophobic substrate. *Proc. Natl. Acad. Sci. U.S.A.* **114** (27), 6930–6935.
- SIJS, R. & BONN, D. 2020 The effect of adjuvants on spray droplet size from hydraulic nozzles. *Pest. Manage. Sci.* **76** (10), 3487–3494.
- SMITH, F. R. & BRUTIN, D. 2018 Wetting and spreading of human blood: recent advances and applications. *Curr. Opin. Colloid Interface Sci.* **36**, 78–83.
- SMITH, F. R., NICLOUX, C. & BRUTIN, D. 2018 Influence of the impact energy on the pattern of blood drip stains. *Phys. Rev. Fluids* **3** (1), 013601.

- 670 SMITH, M. I. & BERTOLA, V. 2010 Effect of polymer additives on the wetting of impacting  
671 droplets. *Phys. Rev. Lett.* **104**, 154502.
- 672 SOTO, D., DE LARIVIERE, A. B., BOUTILLON, X., CLANET, C. & QUÉRÉ, D. 2014 The force  
673 of impacting rain. *Soft Matter* **10** (27), 4929–4934.
- 674 SPRITTLER, JAMES E 2024 Gas microfilms in droplet dynamics: When do drops bounce? *Annu.  
675 Rev. Fluid Mech.* **56**, 91–118.
- 676 THORAVAL, M.-J., SCHUBERT, J., KARPITSCHKA, S., CHANANA, M., BOYER, F., SANDOVAL-  
677 NAVAL, E., DIJKSMAN, J. F., SNOEIJER, J. H. & LOHSE, D. 2021 Nanoscopic interactions  
678 of colloidal particles can suppress millimetre drop splashing. *Soft Matter* **17** (20), 5116–  
679 5121.
- 680 THORAVAL, M.-J., TAKEHARA, K., ETOH, T. G. & THORODDSEN, S. T. 2013 Drop impact  
681 entrapment of bubble rings. *J. Fluid Mech.* **724**, 234–258.
- 682 TSAI, P., LAMMERTINK, R. G. H., WESSLING, M. & LOHSE, D. 2010 Evaporation-triggered  
683 wetting transition for water droplets upon hydrophobic microstructures. *Phys. Rev. Lett.*  
684 **104** (11), 116102.
- 685 TUTEJA, A., CHOI, W., MA, M., MABRY, J. M., MAZZELLA, S. A., RUTLEDGE, G. C.,  
686 MCKINLEY, G. H. & COHEN, R. E. 2007 Designing superoleophobic surfaces. *Science*  
687 **318** (5856), 1618–1622.
- 688 VILLERMAUX, E. 2020 Fragmentation versus cohesion. *J. Fluid Mech.* **898**, P1.
- 689 VILLERMAUX, E. & BOSSA, B. 2011 Drop fragmentation on impact. *J. Fluid Mech.* **668**, 412–  
690 435.
- 691 VILLERMAUX, E., WANG, X. & DEIKE, L. 2022 Bubbles spray aerosols: certitudes and mysteries.  
692 *Proc. Natl. Acad. Sci. Nexus* **1** (5), pgac261.
- 693 VOLK, A. & KÄHLER, C. J. 2018 Density model for aqueous glycerol solutions. *Exp. Fluids*  
694 **59** (5), 75.
- 695 WAGNER, H. 1932 Über Stoß- und Gleitvorgänge an der Oberfläche von Flüssigkeiten. *Z. Angew.  
696 Math. Mech.* **12** (4), 193–215.
- 697 WILDEMAN, S., VISSER, C. W., SUN, C. & LOHSE, D. 2016 On the spreading of impacting  
698 drops. *J. Fluid Mech.* **805**, 636–655.
- 699 WORTHINGTON, A. M. 1876a On the forms assumed by drops of liquids falling vertically on a  
700 horizontal plate. *Proc. R. Soc.* **25** (171–178), 261–272.
- 701 WORTHINGTON, A. M. 1876b A second paper on the forms assumed by drops of liquids falling  
702 vertically on a horizontal plate. *Proc. R. Soc.* **25** (171–178), 498–503.
- 703 WU, S., DU, Y., ALSAID, Y., WU, D., HUA, M., YAN, Y., YAO, B., MA, Y., ZHU, X. & HE,  
704 X. 2020 Superhydrophobic photothermal icephobic surfaces based on candle soot. *Proc.  
705 Natl Acad. Sci. USA* **117** (21), 11240–11246.
- 706 XU, L., ZHANG, W. W. & NAGEL, S. R. 2005 Drop splashing on a dry smooth surface. *Phys.  
707 Rev. Lett.* **94** (18), 184505.
- 708 YARIN, A. L. 2006 Drop impact dynamics: splashing, spreading, receding, bouncing... *Annu.  
709 Rev. Fluid Mech.* **38**, 159–192.
- 710 YARIN, A. L., ROISMAN, I. V. & TROPEA, C. 2017 *Collision Phenomena in Liquids and Solids*.  
711 Cambridge University Press.
- 712 YUN, S. 2017 Bouncing of an ellipsoidal drop on a superhydrophobic surface. *Sci. Rep.* **7** (1),  
713 17699.
- 714 ZHANG, B., LI, J., GUO, P. & LV, Q. 2017 Experimental studies on the effect of reynolds and  
715 weber numbers on the impact forces of low-speed droplets colliding with a solid surface.  
716 *Exp. Fluids* **58** (9), 1–12.
- 717 ZHANG, B., SANJAY, V., SHI, S., ZHAO, Y., LV, C. & LOHSE, D. 2022 Impact forces of water  
718 drops falling on superhydrophobic surfaces. *Phys. Rev. Lett.* **129**, 104501.
- 719 ZHANG, R., ZHANG, B., LV, Q., LI, J. & GUO, P. 2019 Effects of droplet shape on impact  
720 force of low-speed droplets colliding with solid surface. *Exp. Fluids* **60** (4), 64.
- 721 ZHENG, S., DILLAVOU, S. & KOLINSKI, J. M. 2021 Air mediates the impact of a compliant  
722 hemisphere on a rigid smooth surface. *Soft Matter* **17** (14), 3813–3819.